University of Twente

Health Technology Implementation
Master Thesis

Non-Contact Measurement of Heart Rate Independent of Skin Tone and Environment Light Using Near-Infrared Illumination

Student:
M.J.H. Gringhuis

Supervisor:
prof.dr.ir. R.M. Verdaasdonk

Examination Committee:
dr.ir. F.H.C. de Jongh
prof.dr.ir. N. Bosschaart

16-04-2024

Contents

Declaration of the Usage of AI

I hereby declare that I have composed this work independently and with the use ChatGPT and Grammarly. After a constructive discussion with the examination committee it was decided to use artificial intelligence (AI) to increase the readability of this thesis and to eliminate any spelling errors. I acknowledge that while AI technologies have contributed to the refinement of the written content, they have been applied selectively and with discretion, focusing solely on enhancing readability and ensuring linguistic accuracy. The core research methodologies, data analysis, and interpretation presented in this thesis have not been influenced or determined by AI algorithms.

M.J.H. Gringhuis, 16-04-2024

Abstract

Newborns requiring intensive medical care are placed in a specialized area of the hospital known as the neonatal intensive care unit (NICU). In the NICU, electrocardiography (ECG) is employed to continuously monitor heart function. Due to the delicate nature of infants' skin epidermis, removing ECG electrodes can result in skin lesions and discomfort for the infant, causing pain and disrupting sleep. Introducing a reliable, contactless measurement technique could significantly enhance comfort levels for neonates in a NICU.

Remote photoplethysmography (rPPG) is an contactless technology that utilizes video recordings of individuals to extract vital health parameters, such as heart rate. This thesis explores the functionality and reliability of near-infrared remote photoplethysmography (NIR-rPPG) for non-contact heart rate measurement, irrespective of skin tone and environmental lighting conditions. NIR-rPPG is particularly intriguing due to its potential to operate without disrupting sleep and its likely independence from variations in skin tone compared to ambient rPPG. Additionally, a Python-based rPPG application will be developed.

The rPPG application will undergo optimization initially on a single test subject to assess the impact of factors such as camera type, noise, motion artifacts, environmental lighting, and stability. Subsequently, tests will be conducted with eighteen human test subjects representing all skin types according to the Fitzpatrick skin type classification. The experimental procedures were approved by the ethics committee of the University of Twente (application nr. 230114). Heart rate error (HRE), signal-to-noise ratio (SNR), and analysis of variance (ANOVA) will be utilized to interpret the results.

During the human subject experiments, our rPPG application demonstrated independence from variations in skin tone and environmental lighting under NIR conditions. The heart rate error was found to be within a 95% confidence interval ranging from -6.1% to 6.2%. Additionally, a demonstrator resembling a mirror was developed for heart rate measurement purposes. Through optimization, we identified the optimal parameters and settings within the scope of this research. The HQCAM was chosen as the camera for experiments with human subjects. Furthermore, after evaluating various rPPG algorithms, the POS algorithm emerged as the most promising option under NIR conditions.

1 Introduction

1.1 Heart Rate Measurement as Indicator for Health

The well-being of an individual can be evaluated by monitoring various physiological parameters, including heart rate, blood pressure, respiration rate, and blood oxygenation [1]. These measurable biological functions offer valuable insights into an individual's cardiorespiratory stability and overall health. Established limits have been defined for these parameters to delineate normal ranges in healthy individuals. Moreover, monitoring physiological parameters serves not only to diagnose diseases but also to identify potential health risks. In this thesis, particular emphasis will be placed on heart rate, which serves as a reliable indicator of human health during resting conditions.

Heart rate stands out as a crucial physiological parameter due to the indispensable role of the heart in sustaining bodily functions. Responsible for circulating oxygen and nutrient-rich blood throughout the body, the heart also facilitates the removal of carbon dioxide and waste products [2]. Additionally, heart rate serves as a valuable diagnostic tool for various diseases. Tachycardia may signal underlying health issues such as infection, cardiomyopathy, or hypokalemia [3][4][5]. Conversely, bradycardia could indicate conditions like Lyme disease or hyperkalemia [6][7]. However, it's important to note that an elevated or reduced heart rate isn't always indicative of a health problem; fluctuations occur naturally, such as during sleep or periods of excitement.

The measurement of heart rate dates back to around 300 B.C., credited to the ancient Greeks, Chinese, or Indians, who palpated the subject's pulse at a major artery using their fingers [8]. However, it wasn't until 1707 that clinical assessment of heart rate became feasible with the invention of the "Physicians Pulse Watch," equipped with two sets of hands, one of which could be stopped to function as a timer [9]. A significant milestone occurred in the 1920s with the development of the first electrocardiogram (ECG) device by Dutch physiologist Willem Einthoven [10]. The introduction of the ECG marked a monumental breakthrough in the scientific community's ability to analyze heart function. Over time, continuous improvements have been made to ECG technology, rendering it an indispensable component of the initial evaluation of patients with cardiovascular health issues [11].

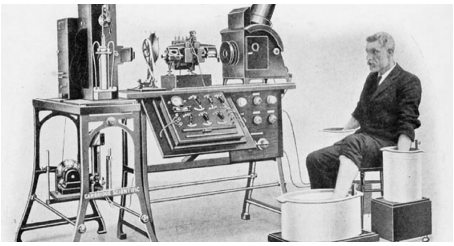

Figure 1: Willem Einthoven with one of the first commercially available ECG devices. Source: [12]

Over the past few decades, extensive research has been dedicated to photoplethysmography (PPG), a non-invasive method derived from the Greek words "photos" (light), "plethysmos" (increasing), and "graphein" (to write) [13]. PPG operates by measuring changes in blood volume within tissues using light, detectable via a photodetector. Figure 2 illustrates a schematic representation of a finger pulse oximeter, a device employing PPG to measure heart rate, blood oxygen saturation, and respiration rate. Typically, finger pulse oximeters utilize two LEDs emitting light at 690 nm (red) and 940 nm (infrared) wavelengths [14]. Widely employed in sports medicine, medical diagnostics, and wearable technology, PPG offers several advantages over traditional methods for measuring physiological parameters, including its non-invasiveness and greater comfort for patients [15]. Moreover, with the proliferation of wearable devices integrated into daily attire, PPG has emerged as a pivotal technology for real-time tracking of health and fitness parameters.

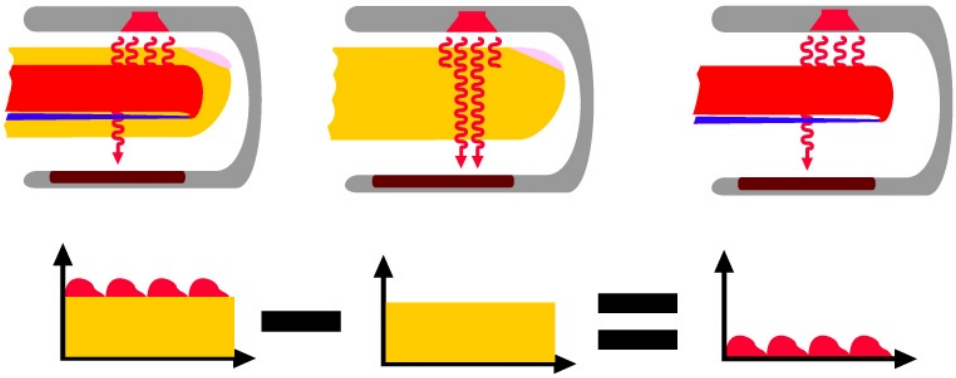

Figure 2: A schematic depiction illustrating the operational principle of a finger pulse oximeter. With each heartbeat, blood is propelled throughout the body, filling the blood vessels, thereby causing a slight increase in volume. Conversely, between heartbeats, the volume diminishes. These minute fluctuations in volume induce alterations in the transmission of light through the tissue. Despite their subtle nature, these variations can be detected and quantified by a pulse oximeter utilizing photoplethysmography. Source: [16]

1.2 Remote Photoplethysmography

Remote photoplethysmography (rPPG) represents the non-contact adaptation of traditional photoplethysmography (PPG). This method enables the measurement of physiological parameters such as heart rate, oxygen saturation, and respiration rate from a distance [17]. Utilizing a video camera, rPPG captures subtle variations in skin color attributed to changes in blood volume, thereby reflecting alterations in heart rate and various other physiological parameters. Typically, ambient light serves as the primary illumination source for rPPG. In recent years, rPPG has garnered considerable interest as a promising technology for remote health monitoring, sports performance analysis, and numerous other applications [18]. However, owing to the delicate nature of the changes in skin color induced by fluctuations in blood volume, the rPPG signal extracted from video data tends to be weak. Motion artifacts and suboptimal lighting conditions can introduce noise into the rPPG signal, thereby compromising its reliability. Moreover, individuals with darker skin tones exhibit lesser variations in skin color under ambient conditions compared to those with lighter skin tones, leading to a comparatively weaker rPPG signal in darker skin types [19].

To mitigate the weaker signal of rPPG in individuals with darker skin tones, our focus will be on near-infrared remote photoplethysmography (NIR-rPPG). Near-infrared (NIR) wavelengths, ranging from 800 to 2500 nm, lie just beyond the red light in the electromagnetic spectrum and are imperceptible to the human eye (see Figure 3). We hypothesize that NIR-rPPG exhibits greater resilience to darker skin types compared to ambient rPPG due to the diminished absorption of NIR light by melanin, the pigment in the skin, in contrast to visible light [19]. Consequently, NIR light can penetrate deeper into dark skin, potentially yielding a stronger rPPG signal relative to noise. Moreover, NIR-rPPG proves particularly advantageous in scenarios where traditional rPPG may falter, such as during sleep in dark environments. Research has shown that NIR-rPPG reliably captures heart rate and blood oxygen saturation readings across diverse settings, including low-light conditions and individuals with varying skin tones [20]. In this thesis we will look at NIR-rPPG in the wavelength range from around 800 nm to 1000 nm.

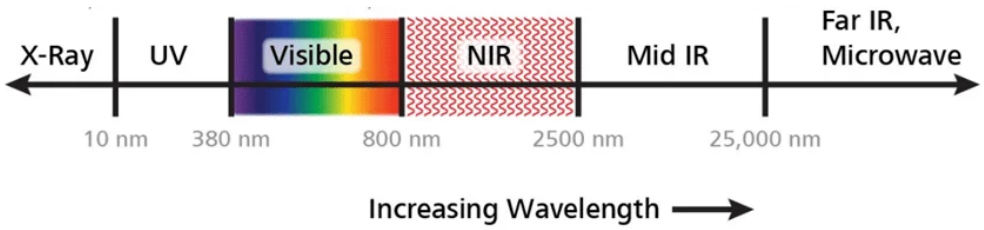

Figure 3: A representation of the electromagnetic spectrum. It shows that near infrared illumination has a higher wavelength than visible illumination. Source: [21]

1.3 Heart Rate Monitoring in Neonatal Intensive Care Units

Newborn infants requiring intensive medical attention are admitted to a specialized unit within hospitals known as the Neonatal Intensive Care Unit (NICU). Typically, infants admitted to the NICU are either born prematurely, have low birth weight, or exhibit medical conditions necessitating specialized care. In this critical care setting, the continuous monitoring of cardiorespiratory stability is paramount, particularly for preterm infants [22]. Throughout their hospitalization in the NICU, vital signs are continuously monitored to ensure optimal care. These vital signs encompass parameters such as heart rate, respiratory rate, pulse oximetry readings, and blood pressure [23]. Such meticulous monitoring aids in early detection of any fluctuations or abnormalities in the infant's physiological status, enabling prompt intervention and management when necessary.

In the NICU, continuous monitoring of cardiac activity is achieved through the use of ECG [24]. ECG functions by detecting the electrical impulses generated by the heart muscle during depolarization, which propagate as electrical signals to the skin's surface. These signals are captured by electrodes affixed to the infant's chest, as depicted in Figure 4. The skin of infants is notably delicate, making the removal of ECG electrodes a potential source of discomfort and pain for the infant [25][26]. Additionally, the presence of electrodes can disrupt the infant's sleep patterns, further complicating their care. rPPG presents a promising alternative to traditional ECG monitoring, potentially mitigating the challenges associated with electrode use. However, it is important to note that while rPPG offers advantages in terms of comfort and sleep quality for infants, it cannot fully replace ECG due to its inability to provide comprehensive monitoring of cardiac function.

Figure 4: A picture demonstrating how the electrodes of the ECG are connected to a baby. Source: [27]

Throughout the duration of this research, a novel device known as the Bambi Belt, developed by Bambi Medical based in Eindhoven, was investigated for its efficacy in cardiorespiratory monitoring. The Bambi Belt represents a wireless, non-adhesive sensor belt, which under-

went extensive testing at both the Máxima Medical Centre in Eindhoven and the Academic Medical Centre in Amsterdam. Results from these trials revealed that the Bambi Belt demonstrated non-inferiority in heart rate monitoring when compared to the standard ECG method employing adhesive electrodes, particularly in testing involving infants [28]. Moreover, observations indicated that prolonged utilization of the Bambi Belt was associated with fewer adverse effects on skin conditions in preterm infants, in contrast to the utilization of traditional adhesive electrodes [29]. These findings underscore the potential of the Bambi Belt as a promising alternative for cardiorespiratory monitoring, offering enhanced comfort and reduced skin-related complications for infants in clinical settings.

1.4 Aims of this Research

This thesis aims to create a rPPG implementation in Python software code that functions under NIR-lighting conditions and for every skin colour. Therefore, several pre-existing rPPG scripts are incorporated, translated and adapted. Moreover, the implementation will be optimized, validated and tested with test subjects and newly available NIR-sensitive cameras. Finally, a demonstrator will be designed and produced that can be used at Open Days at the University of Twente.
To be able to reach these goals, some research questions have been formulated:

- Is rPPG a feasible method for non-contact heart rate measurement independent of skin tone and environment light using near-infrared illumination?
- Which rPPG method performs the best under NIR conditions?
- Which rPPG method performs the best independent of skin tone?

The following are the new aspects that this thesis adds to the rPPG research:

- A real-time software implementation of core rPPG algorithms into one Python application.
- The use of RGB-cameras modified to NIR sensitive cameras.
- The use of a new rPPG method optimized for NIR light.
- Evaluation of the application by testing on humans with different skin tones.
- The creation of a demonstrator.

2 Theory

2.1 The Optics behind Photoplethysmography

2.1.1 Skin Chromophores and the Light-Tissue Interaction

Since rPPG relies on detecting subtle changes in skin coloration, understanding the role of skin chromophores is crucial. Chromophores are particles within tissues that influence their coloration. In human skin tissue, the primary chromophores responsible for absorbing short-wavelength near-infrared light include melanin, water, oxyhemoglobin, and deoxyhemoglobin [30]. The absorption coefficient of these chromophores varies across different wavelengths, as depicted in Figure 5. Water, being the most abundant chromophore, is uniformly distributed throughout human tissues. However, significant absorption of light by water occurs only at higher wavelengths, typically above 1200 nm [31]. This suggests that water does not significantly influence NIR-rPPG measurements under 1200 nm.

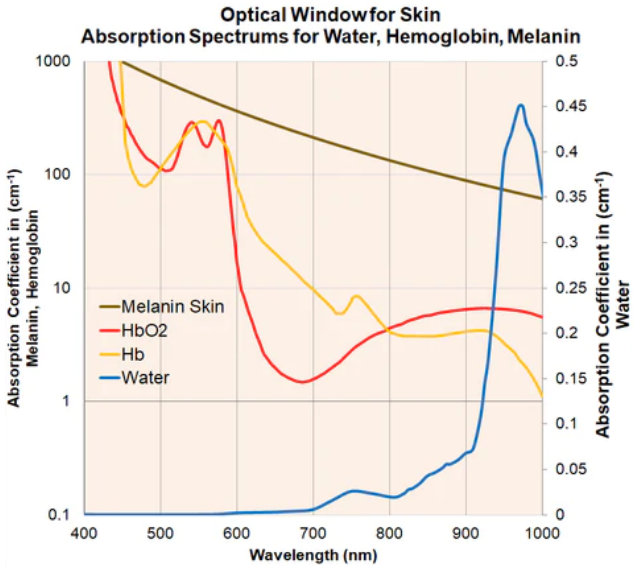

Figure 5: The absorption spectrum of the main chromophores in human skin tissue. Source: [32]

Melanin, the primary chromophore in human skin tissue, largely determines skin coloration [33]. The Fitzpatrick scale provides a classification system for human skin types based on constitutive skin pigmentation and the ability to tan in sunlight, as depicted in Figure 6 [34]. Two types of melanin are significant contributors to the color of human skin tissue: eumelanin and pheomelanin [33]. Eumelanin, responsible for darker tones, contrasts with pheomelanin, which imparts more pinkish tones. The unique combination of these melanin types determines an individual's skin color. While all individuals generally possess the same number of melanocytes (cells responsible for melanin production), the amount of melanin

produced varies. Higher levels of melanin production result in darker skin, hair, and eye colors.

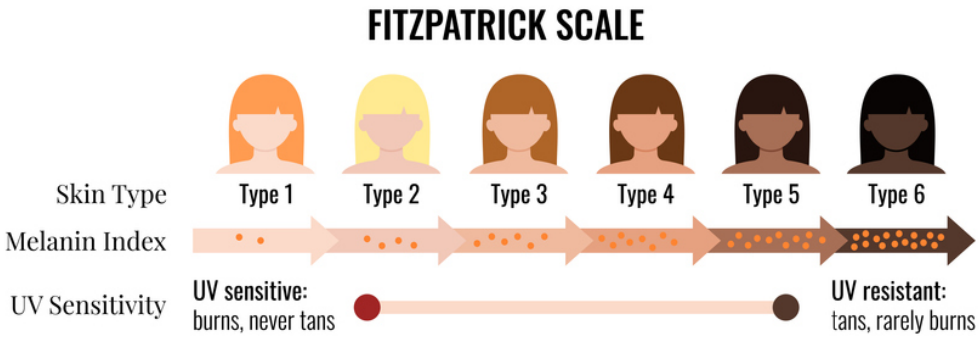

Figure 6: The Fitzpatrick skin types classifications. Source: [35]

The absorption spectra of skin chromophores reveal an optical window wherein visible and near-infrared light can effectively penetrate tissue for blood flow or volume measurements [36]. This optical window arises from the strong absorption of light by water in the ultraviolet and longer infrared wavelengths, as well as by melanin at shorter wavelengths. The wavelength of light plays a crucial role in its interaction with tissue [37]. Tissue penetration depth, defined as the depth to which light can penetrate tissue for a given intensity, varies based on the wavelength of light, as illustrated in Figure 7. The absorption coefficient of melanin decreases as the wavelength increases within the range of 400 to 1000 nm [38]. For instance, the absorption coefficient of melanin reduces from approximately 600 cm^{-1} at 600 nm to about 90 cm^{-1} at 940 nm. This reduction in absorption coefficient suggests that the rPPG signal at near-infrared wavelengths would be stronger for darker skin types due to lesser light absorption compared to visible wavelengths.

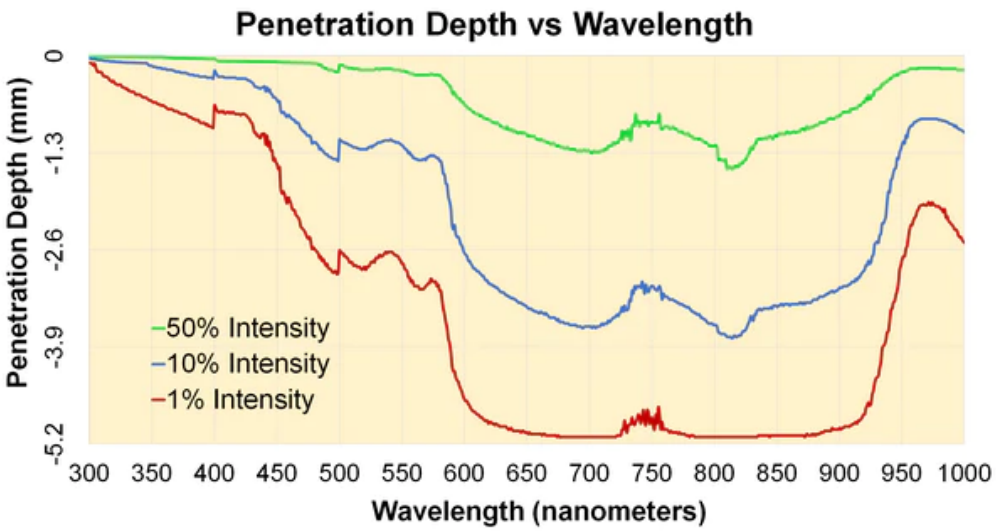

Figure 7: The penetration depth of different wavelengths of light into human skin tissue shown per 50%, 10% and 1% of the light intensity that reaches that depth. Source: [39]

Blood flow is essential for delivering oxygen to all parts of the human body. Haemoglobin molecules, present in red blood cells, contain four heme groups capable of binding oxygen molecules. When oxygen is bound to a haemoglobin molecule, it forms oxyhemoglobin (HbO_2), whereas when no oxygen is bound, it is referred to as deoxyhemoglobin (Hb). The presence or absence of oxygen binding influences the absorption profile of haemoglobin, as depicted in Figure 5. Wavelengths near 805 nm are termed isosbestic wavelengths. At these wavelengths, there are minimal differences in absorption between oxyhemoglobin and deoxyhemoglobin [40]. Consequently, the signal remains largely unaffected by changes in oxygen saturation. Pulse oximeters, commonly used for measuring blood oxygenation, typically utilize one non-isosbestic wavelength and one isosbestic wavelength to calculate oxygen saturation levels [41].

2.1.2 The Dichromatic Reflectance Model

To delve into the principles underlying pulse extraction in rPPG methods, it's essential to begin by summarizing the dichromatic reflectance model, which defines the optical and physiological properties of skin reflections. This model provides valuable insights into the challenges encountered in rPPG usage and how various rPPG methods address these challenges.

The signal captured by a digital camera comprises both specular reflections and diffuse reflections, as described in the dichromatic reflectance model [42][43]. Specular reflection refers to the mirror-like reflection of waves, such as light, from a surface. However, specular reflections typically lack meaningful physiological information relevant to rPPG analysis. In contrast, diffuse reflection in rPPG refers to light that penetrates the skin, scatters within the deeper layers of tissue, and is either absorbed or emitted back out of the body. Variations in the diffuse reflection component are primarily induced by the cardiac cycle, as blood

exhibits stronger light absorption compared to surrounding tissues [44]. The degree of light absorption is directly proportional to the volume of blood flowing through the tissue's blood vessels. Consequently, changes in blood volume lead to alterations in the color of the diffuse reflection [45].

Now, imagine a scenario where a light source illuminates a piece of human skin tissue, and there is a pulsating blood flow within this piece of skin. Simultaneously, a remote camera captures this illuminated skin tissue, depicted in Figure 8. Additionally, we assume that the light source emits light of a consistent spectral composition. The distance between the light source and the skin tissue and the distance between the skin tissue and the sensors inside the camera will influence the intensity the camera detects. So, the skin captured by the camera has a specific intensity that changes over time. These variations in intensity are caused by both motion-induced specular changes and subtle colour shifts induced by the pulse. The extent of these temporal changes is directly related to the luminance intensity level.

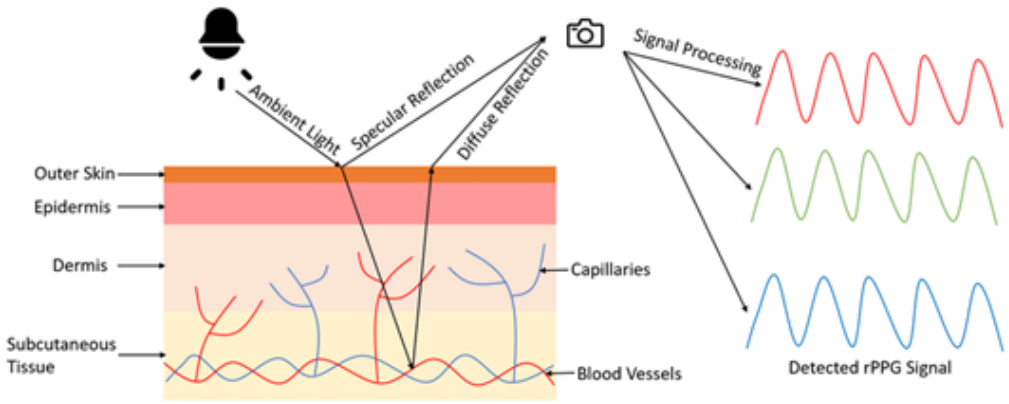

Figure 8: A schematic representation of the dichromatic reflectance model. Source: [42]

Using the dichromatic model, the reflection of each skin pixel in a recorded image sequence by the RGB channels can be represented as a time-dependent function:

$$S_k(t) = I(t) \cdot (v_s(t) + v_d(t)) + v_n(t), \tag{2.1}$$

where $S_k(t)$ stands for the RGB channels in a column of the k-th pixel; I(t) represents the luminance intensity level, accounting for the variations in intensity caused by the light source and the relative distances between the light source, skin tissue and camera. I(t) is modulated by the specular reflection $v_s(t)$ and the diffuse reflection $v_d(t)$. The quantization noise of the camera sensors is represented by $v_n(t)$. The time-dependent nature of the components results from both the body's motion and the pulsatile blood flow.

Specular reflections refer to the mirror-like reflection of the light from the skin tissue; this light does not contain any pulsatile information. Hence, the spectral composition of the specular reflection remains the same as that of the light source. The component varies over time due to the influence of body motion; this affects the geometric relationship between the

light source, skin surface and the camera. The specular reflection component can be written as:

$$v_s(t) = u_s \cdot (s_0 + s(t)), \tag{2.2}$$

here u_s represents the unit colour vector of the light spectrum of the light source. The s_0 and s(t) components refer to the stationary and varying parts of the specular reflections, respectively. The motion of the body specifically induces the s(t) component.

Whereas the specular reflection contains no pulsatile information, the diffuse reflection does contain information about the pulsatile flow of the blood. The diffusely reflected light is connected to the absorption and scattering of the light within the skin tissues. The haemoglobin and melanin levels in the blood and skin influence the chromaticity of the diffuse reflection component. This means that the diffuse reflection component varies due to changes in the blood volume and is, therefore, time-dependent. We represent this time dependency as:

$$v_d(t) = u_d \cdot d_0 + u_p \cdot p(t), \tag{2.3}$$

u_d refers to the unit colour vector of the skin tissue; d_0 stands for the stationary reflection strength; u_p denotes the relative pulsatile strengths in the RGB channels; and p(t) stands for the pulse signal.

When we substitute Equation 2.2 and Equation 2.3 into Equation 2.1, we receive the following formula:

$$S_k(t) = I(t) \cdot \Big(u_s \cdot (s_0 + s(t)) + u_d \cdot d_0 + u_p \cdot p(t)\Big) + v_n(t). \tag{2.4}$$

From Equation 2.4, we can take the stationary parts of both the specular reflection component and the diffuse reflection component; this will represent the stationary skin reflection:

$$u_c \cdot c_0 = u_s \cdot s_0 + u_d \cdot d_0, \tag{2.5}$$

here u_c represents the unit colour vector of the skin reflection, and c_0 stands for the reflection strength.

Now we are able to rewrite Equation 2.4 into:

$$S_k(t) = I_0 \cdot \Big(1 + i(t)\Big) \cdot \Big(u_c \cdot c_0 + u_s \cdot s(t) + u_p \cdot p(t)\Big) + v_n(t), \tag{2.6}$$

the luminance intensity level I(t) is expressed as a combination of the stationary part I_0 and a time-varying part $I_0 \cdot i(t)$. It's important to note that the specular reflection component can be significantly larger than the other components, overpowering them. To address this, we assume the existence of means to negate the pixels where the specular reflection dominates. Furthermore, polarization could also help solve this problem; a polarization filter could be placed in front of the light source and the camera. Only diffusely reflected light would then reach the sensor of the camera.

From the dichromatic model and the model Equation 2.6, it becomes apparent that we want to extract the pulsatile component p(t) from the colour information S_k(t).

2.1.3 The rPPG Signal

The rPPG signal can be divided into an AC and a DC component; see Figure 9 [44]. The AC component is the pulsatile component p(t) of the rPPG waveform and usually has its fundamental frequency around 1 Hz. This AC component is superimposed onto a large DC component. The DC component relates to the tissues and the average blood volume in the tissue; this component varies slowly due to vasomotor activity, respiration, thermoregulation and other physiological processes. These characters are dependent on where on the body the rPPG signal is recorded [46].

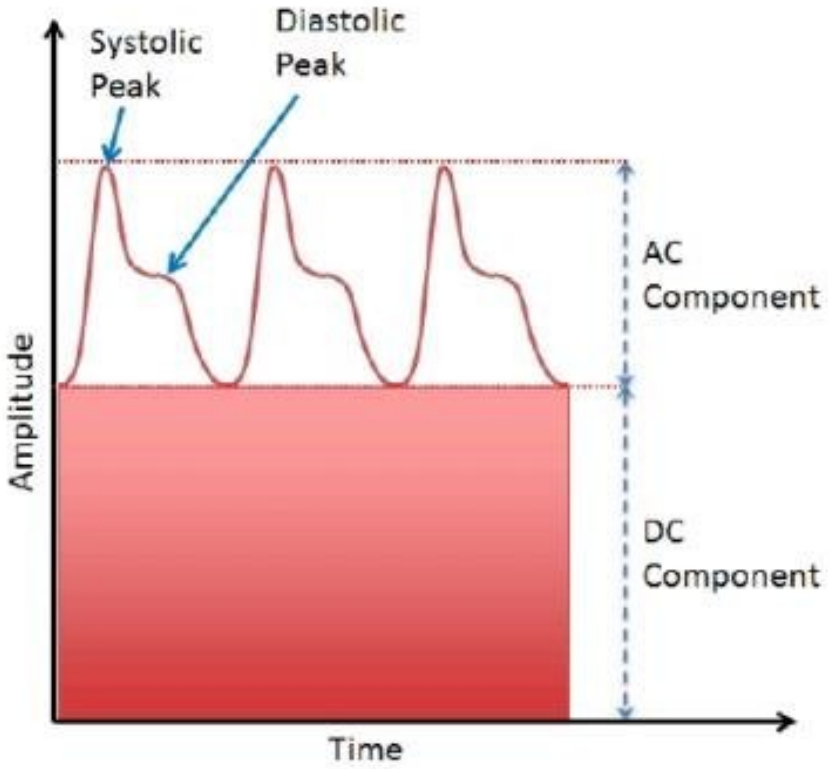

Figure 9: A depiction of a perfect rPPG signal, with at the bottom the DC component and superimposed on top of this the AC component. Source: [47]

The main factors influencing the AC component are the blood volume and the blood vessel wall movement [48]. The amount of blood in the vessel and the position of the blood vessel wall influence how the light is reflected and the amount of light that is captured by the camera. So, the recorded rPPG pulses directly correlate with the tissue perfusion that the camera is pointed on [49].

It should be noted that extracting the PPG signal in the NIR wavelength range presents significantly greater challenges compared to the RGB wavelength region, primarily due to two physiological reasons [20]. Firstly, the pulsatile strength (AC/DC ratio) in NIR is no-

tably lower than in RGB, attributed to the lower spectral absorption of hemoglobin in the NIR wavelength range. Secondly, the pulsatile contrast between different NIR wavelengths is smaller because the blood absorption spectrum in NIR is flatter than that in RGB. These factors contribute to strong disturbances that can easily disrupt the pulsatile component, making it challenging to separate from these disturbances during signal extraction processes.

2.2 The rPPG Pipeline

2.2.1 Analysis of State-of-the-art Core rPPG Algorithms

In order to design our Python implementation effectively, a thorough understanding of the evolution and advancements in rPPG technology and algorithms is crucial. To accomplish this, a comprehensive review of relevant literature was conducted prior to initiating the project. This review process yielded the process flow depicted in Figure 10.
A typical rPPG processing chain comprises several key components, including region of interest (ROI) selection, signal pre-processing, and the core algorithm for extracting the rPPG signal. More sophisticated rPPG pipelines may also incorporate ROI tracking and post-filtering of the signal. These building blocks collectively form the foundation of rPPG technology and play integral roles in its successful implementation and utilization.

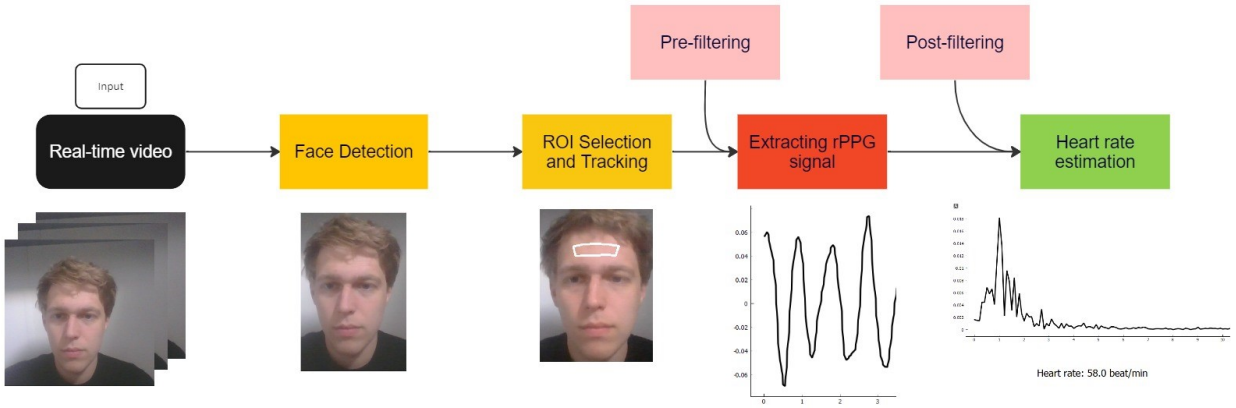

Figure 10: A generalized pipeline of a rPPG algorithm.

2.2.2 Region of Interest Detection Methods

To detect a person's heart rate from a real-time video, it's essential to first detect the person's face, as the face often serves as the region of interest. Two commonly used methods for detecting ROIs in Python are Haar cascade and MediaPipe FaceMesh.

The Haar cascade method utilizes an Object Detection Algorithm to identify faces in images or real-time video [50]. This algorithm relies on edge or line detection features proposed by Viola et al. and is readily available in the OpenCV module of Python [51]. On the other hand, the MediaPipe FaceMesh method, developed by Google, not only locates faces within a frame but also landmarks facial features by outputting 468 3-dimensional face landmarks [52].

While the Haar cascade method is known for its computational efficiency and speed, MediaPipe FaceMesh is preferred for its accuracy and ease of use in facial landmark detection and tracking [53][54]. Despite requiring more processing power than the Haar cascade method, MediaPipe FaceMesh is better suited for our rPPG implementation as it enables a

more accurate definition of the ROI.

2.2.3 Facial Regions of Interest

The information captured by the camera varies depending on the specific area of the face being targeted, primarily due to differences in skin thickness. According to Chen et al., this variation in skin thickness directly influences the depth at which blood vessels are situated [55]. Thicker skin tends to have deeper-seated blood vessels. Based on the findings of Dae-Yael et al., the facial regions most suitable for rPPG signal extraction include the malar regions, the lower medial forehead, and the glabella [56]. These regions have been highlighted in Figure 11. These areas are particularly conducive to rPPG signal extraction due to their relatively thin skin and proximity to superficial blood vessels.

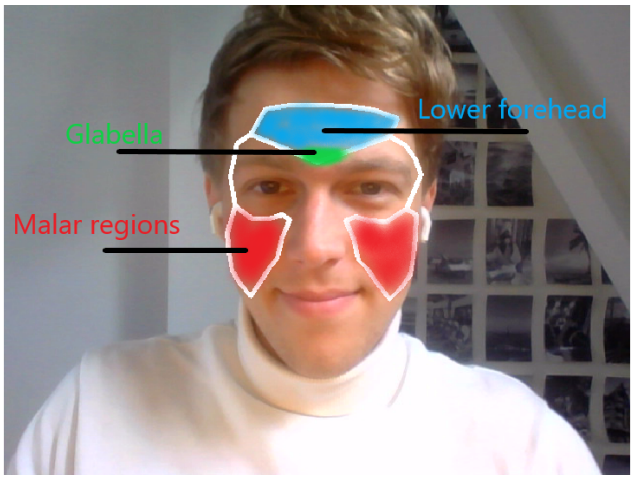

Figure 11: A depiction of the ROI used in this thesis with the malar regions, the lower medial forehead, and the glabella.

2.2.4 rPPG Algorithms

To incorporate the rPPG methods into our Python application, some algorithmic changes had to be made to the available rPPG algorithms. These changes do not affect the nature of the methods. The rPPG methods incorporated into the application can be seen in Figure 12. These are the GREEN method, the POS method, the CHROM method and our own NIR method. Our Python implementation has been built based on an open-source rPPG implementation called yarppg [57]. The GREEN, POS and CHROM methods have been adapted to our implementation, and the NIR method has been added to these existing methods.

Now we will discuss some terminology that will help explain the functioning of the algorithms. Henceforth, we notate $x(t) = (x_r(t), x_g(t), x_b(t))$ as the pre-processed temporal trace in the RGB space. This signal results from inputting the raw RGB signal $s(t)$ in the filtering-based pre-processing stage. So, for the homogeneity of the application, every method will receive a piece of the sequence $x(t)$ as input and produce $y(t)$ as output.

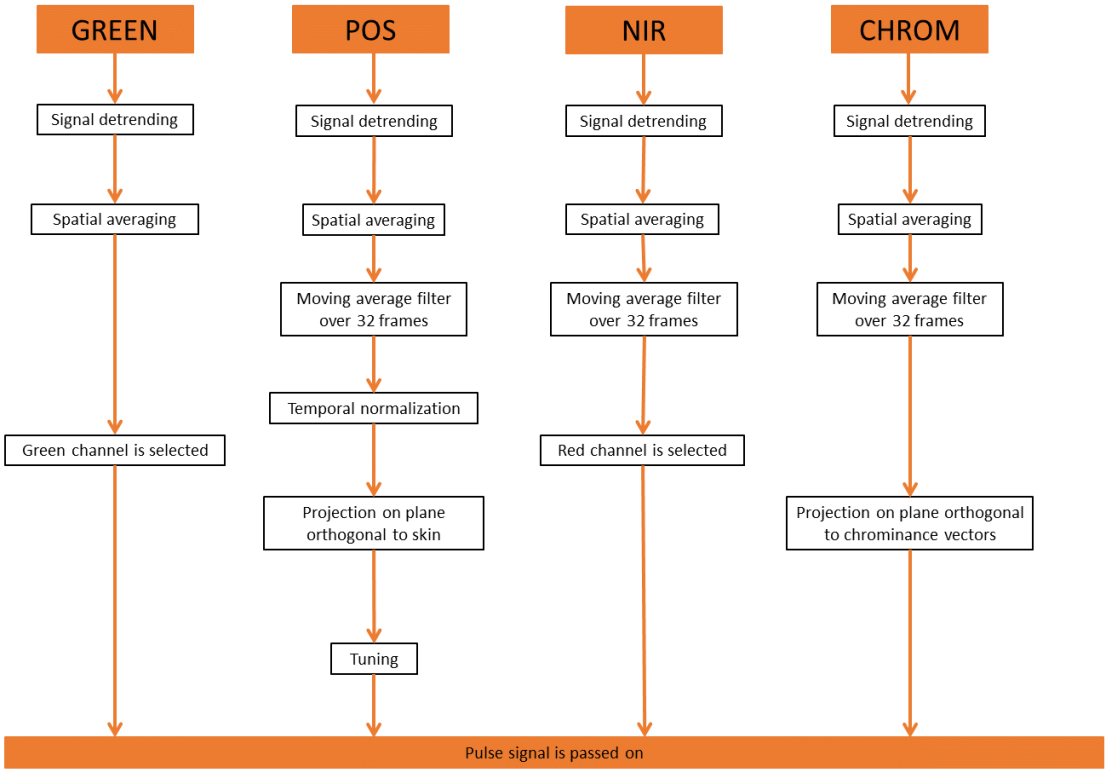

Figure 12: A systematic overview of the GREEN, POS, NIR and CHROM algorithms implemented in the Python application.

2.2.4.1 GREEN

It has been reported in previous works that the green channel provides the strongest plethysmographic signal in the visible wavelength spectrum [58]. This is due to a peak in the absorption spectrum of oxyhemoglobin. The GREEN method is one of the simpler algorithms for estimating the heart rate from the pre-processed temporal trace in the RGB space [59]. The algorithm follows the following steps:

1. The RGB temporal traces are acquired and detrended.
2. The average colour intensity for the green colour channel is calculated.
3. By spatial averaging, the spectral component is extracted. The most dominant frequency is determined and passed on from this spectral component.

So, for the given RGB temporal traces x(t), the GREEN algorithm can be simplified to the following formula: $y(t) = x_g(t)$.

2.2.4.2 CHROM

The chrominance-based (CHROM) algorithm has been designed to try to deal with a weakness that is present in several other rPPG methods: the unpredictability of the errors that are caused during the normalization of the specular reflections at the skin [45]. The light captured by the camera consists of specular and diffuse reflection components. The relative contributions of the components, which together create the observed colour, depend on the angles between the light source, skin, and camera. Thus, these angles vary over time due to the person's motion in front of the camera. This creates a weakness in the rPPG algorithms when the specular component is not eliminated. The CHROM method eliminates the specular component using colour difference or chrominance signals. The algorithm follows the following steps:

1. The RGB temporal traces are acquired, normalized, and detrended.
2. The normalized RGB traces are projected with the following projection matrix:

$$\begin{bmatrix} 3 & -2 & 0 \\ 1.5 & 1 & -1.5 \end{bmatrix}$$

3. This delivers the following two orthogonal chrominance vectors:

$$X_{\text{CHROM}}(t) = 3x_r(t) - 2x_g(t) \tag{2.7}$$

$$Y_{\text{CHROM}}(t) = 1.5x_r(t) + x_g(t) - 1.5x_b(t) \tag{2.8}$$

4. From the following formula, the rPPG signal can be determined:

$$y(t) = X_{\text{CHROM}}(t) - \alpha Y_{\text{CHROM}}(t) \tag{2.9}$$

$$where \;\; \alpha = \frac{\sigma(X_{\text{CHROM}}(t))}{\sigma(Y_{\text{CHROM}}(t))} \tag{2.10}$$

5. By spatial averaging, the spectral component is extracted. The most dominant frequency is determined and passed on from this spectral component.

2.2.4.3 POS

The plane-orthogonal-to-skin (POS) method tries to accomplish the same goal as the CHROM method in eliminating the specular component [59]. However, while pursuing the same goal as the CHROM method, the POS method takes a distinct approach. Instead of focusing solely on analyzing temporal changes in chrominance components, as the CHROM method does, the POS method introduces a novel concept – the creation of a plane orthogonal to the skin tone within the temporally normalized RGB space [60]. This innovative approach capitalizes on the unique characteristics of the RGB color space, where each color component (red, green, blue) can be individually manipulated and analyzed. The projection matrix is orthogonal to the intensity variation direction. By projecting the rPPG signal on the plane orthogonal to the skin tone, the POS method tries to eliminate the specular reflection. This allows for a more precise extraction of physiological signals embedded within the skin color variations, thus improving the overall accuracy and reliability of the rPPG measurements.The algorithm follows the following steps:

1. The RGB temporal traces are acquired, normalized, and detrended.
2. The normalized RGB traces are projected with the following projection matrix:

$$\begin{bmatrix} 0 & 1 & -1 \\ -2 & 1 & 1 \end{bmatrix}$$

3. This delivers the following two orthogonal vectors:

$$X_{\text{POS}}(t) = x_g(t) - x_b(t) \tag{2.11}$$

$$Y_{\text{POS}}(t) = -2x_r(t) + x_g(t) + x_b(t) \tag{2.12}$$

4. The rPPG signal is described by the following formula:

$$y(t) = X_{\text{POS}}(t) + \alpha Y_{\text{POS}}(t) \tag{2.13}$$

$$where \;\; \alpha = \frac{\sigma(X_{\text{POS}}(t))}{\sigma(Y_{\text{POS}}(t))} \tag{2.14}$$

5. By spatial averaging, the spectral component is extracted. The most dominant frequency is determined and passed on from this spectral component.

2.2.4.4 NIR

The near-infrared (NIR) method was thought of in this research. The NIR method is based on the GREEN method in that it only uses the information of one of the colour channels, the red colour channel, of the camera. The red colour channel is used because this channel is the most sensitive to light in the near-infrared wavelength range; see Figure 13a. This piqued our interest to investigate whether this would mean that this channel would then contain more plethysmographic signal than the other channels. The algorithm follows the following steps:

1. The RGB temporal traces are acquired and detrended.
2. The average colour intensity for the red colour channel is calculated.
3. By spatial averaging, the spectral component is extracted. The most dominant frequency is determined and passed on from this spectral component.

So, for the given RGB temporal traces x(t), the NIR algorithm can be simplified to the following formula: $y(t) = x_r(t)$.

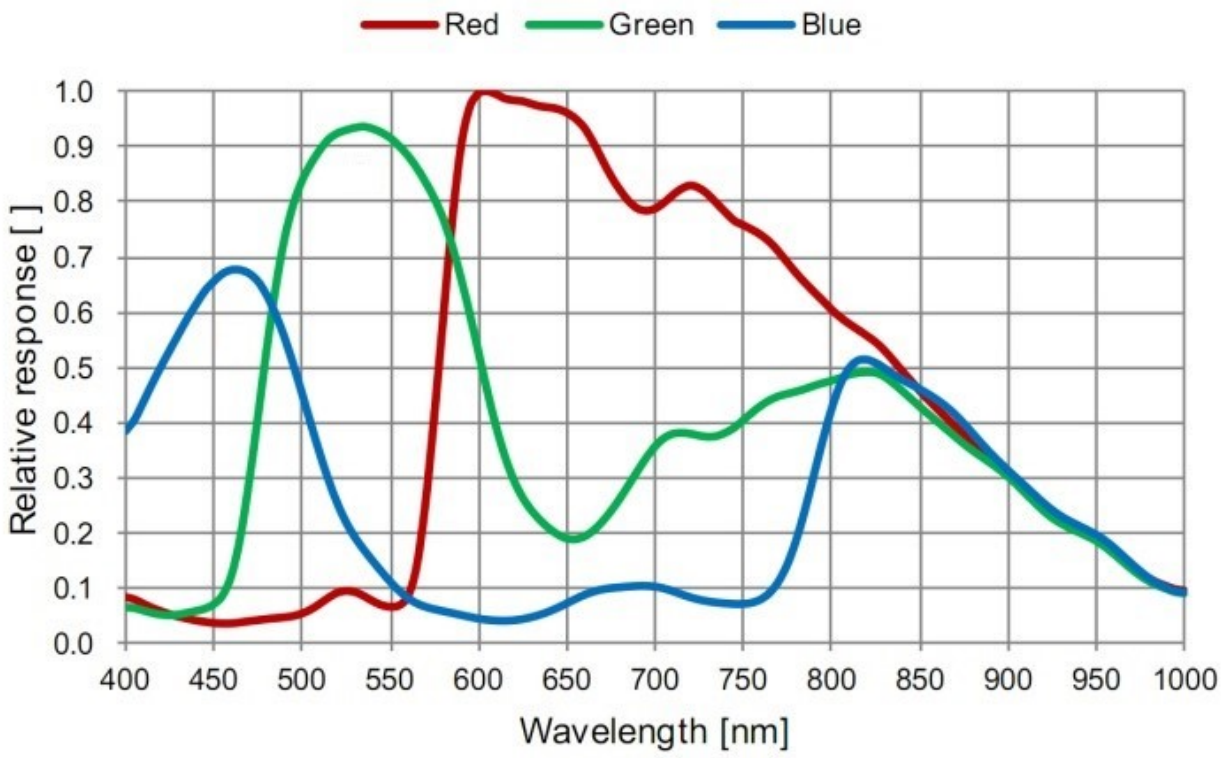

(a) The typical sensitivities of CCD/CMOS sensors and the wavelengths without IR block filter. Source: [61]

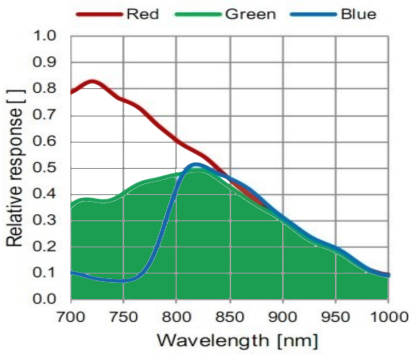

(b) Sensitivity area of the GREEN [62] method in green, which makes use of only the green channel.

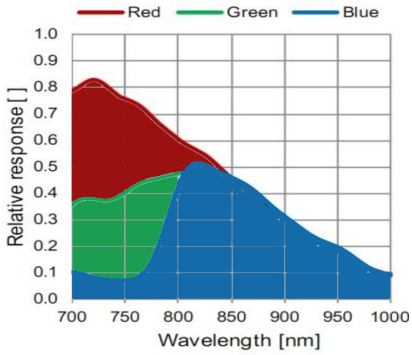

(c) Sensitivity area of the POS [60] and CHROM [45] method in red, green and blue, which make use of all three channels.

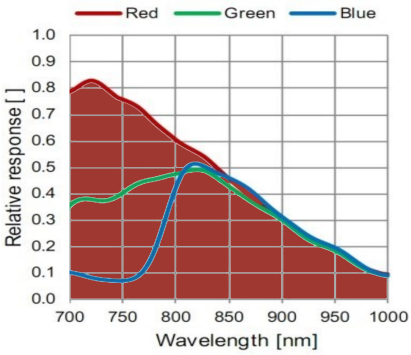

(d) Sensitivity area of the NIR method in red, the NIR method only makes use of the red channel.

Figure 13: The typical sensitivities of CCD/CMOS sensors and accompanying subfigures that zoom in on the NIR range. The subfigures b, c and d show the relative response of the colour channels to the rPPG method in the NIR region.

2.3 Video and Camera Parameters

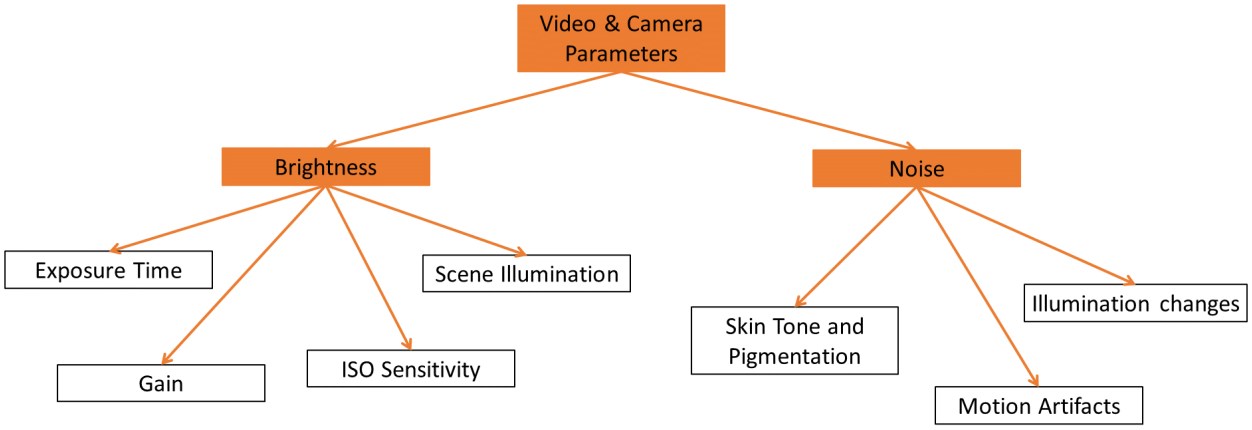

Figure 14: An overview of the video and camera parameters that influence the rPPG signal.

2.3.1 Brightness

Multiple factors influence the brightness and the quality of an image or video. The subsequent equation can represent the relationship between these factors [63]:

$$IB \propto gain * ISO * ET * SI * C \tag{2.15}$$

where IB stands for Image Brightness, gain is the electronic amplification of the detected voltage, ISO stands for the analogue gain, also known as the ISO sensitivity of the camera, ET stands for the exposure time, SI is the scene illumination, and C is a constant that represents factors that are difficult to control, like the reflectivity of objects.

Increasing the gain amplification enhances image brightness, but excessive gain can introduce strong salt-and-pepper noise artefacts [64]. On the other hand, exposure time dictates how long the camera sensor is exposed to light: longer exposure times result in brighter images, but excessive durations may cause motion-blur effects. ISO sensitivity, standardized by the International Organization for Standardization (ISO), represents the camera's sensitivity to light and is quantified as a numerical value [65]. Higher ISO sensitivity values indicate greater light sensitivity and improved light capture capability. Additionally, scene illumination (SI) refers to the intensity of light per unit area, typically measured in lux units. Higher SI values correspond to brighter scenes.

According to Odinaev et al., brightness values below 50 on an 8-bit scale (ranging from 0 to 255) indicate underexposure, while values above 200 indicate overexposure [66]. Their study concluded that increasing video brightness does not significantly reduce the mean absolute error of heart rate estimation. These findings align with the conclusions of van Esch et al., who suggest that controlling exposure time is crucial only to avoid saturation [67].

Moreover, Odinaev et al. found that the best agreement between heart rates calculated from PPG and rPPG signals occurred within a brightness range of 100 to 150 [66]. Additionally, their study revealed that increasing gain did not improve the cross-correlation between heart rates derived from PPG and rPPG signals. These insights emphasize the importance of optimizing brightness levels and exposure settings to achieve accurate heart rate estimation through rPPG methods.

2.3.2 Noise

When acquiring biomedical signals like rPPG, various types of noise accompany the signal. Some of the most common causes of noise from camera electronics in rPPG include:

- **Motion**: Motion of the ROI leads to motion artefacts in the signal. Attempts to minimize this noise often involve ROI tracking techniques [68].
- **Illumination changes**: Variations in illumination cause fluctuations in the brightness of the ROI. Using a uniform light source can help mitigate noise caused by these changes in illumination [68].
- **Skin Tone and Pigmentation**: Variations in skin tone and pigmentation affect how light is absorbed and reflected, resulting in differences in the detected rPPG signal. Darker skin types, such as type VI, tend to exhibit lower signal-to-noise ratio (SNR) values in rPPG measurements compared to lighter skin types [19].

2.4 rPPG Signal Processing

In the processing of the rPPG signal, digital filters play a crucial role in removing or accentuating specific signal characteristics [69]. These filters utilize Fourier transforms to decompose the signal into its frequency components. A Fourier transform converts a signal from the time domain to the frequency domain, providing information about the frequencies present in the original signal. An illustration of a Fourier transform is depicted in Figure 15. Digital filters enable us to isolate specific frequency ranges or eliminate unwanted frequencies from the signal. By allowing certain frequencies to pass through while blocking others, these filters help refine the signal to focus on relevant physiological information. Different types of filters exhibit varying characteristics in terms of signal transmission and blocking.

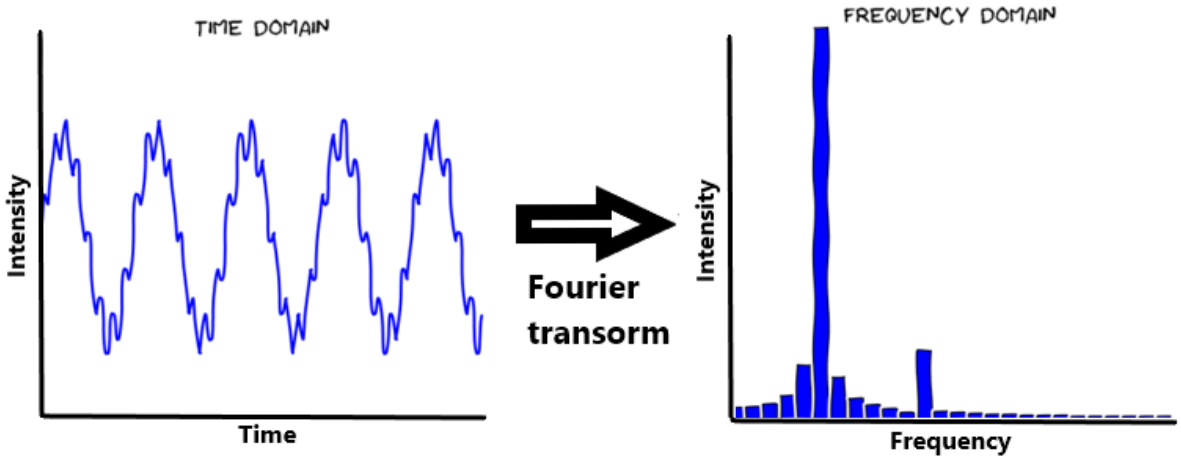

Figure 15: An illustration of a Fourier transform where the signal is transformed from the time domain to the frequency domain. Adapted from: [70]

The cutoff frequency is a crucial characteristic of a filter, determining the frequency at which the filter begins to block or pass the signal. The extent of signal attenuation by the filter depends on its order; higher-order filters typically attenuate the signal more effectively. In rPPG research, most filters used are passband filters, which are defined by lower and upper cutoff frequencies. Frequencies within this passband are allowed to pass through the filter without significant attenuation. Frequencies outside the lower and upper cutoff frequencies fall into the stopband, where the filter attenuates or blocks these frequencies.

2.4.1 Butterworth Filter

The Butterworth filter stands as a pivotal signal-processing tool in rPPG research, effectively managing noise and artefacts within rPPG signals to enhance the accuracy and reliability of extracted physiological information. Often employed as a band-pass filter, the Butterworth filter is engineered to exhibit a maximally flat frequency response within the passband, enabling all band frequencies to traverse without significant attenuation, as depicted in Figure 16 [71]. However, this design characteristic results in a relatively gradual roll-off of frequencies

within the stopband, where frequencies are attenuated. Despite this, the primary objective of the Butterworth filter remains maintaining a smooth response within the passband, albeit at the expense of steeper roll-off characteristics.

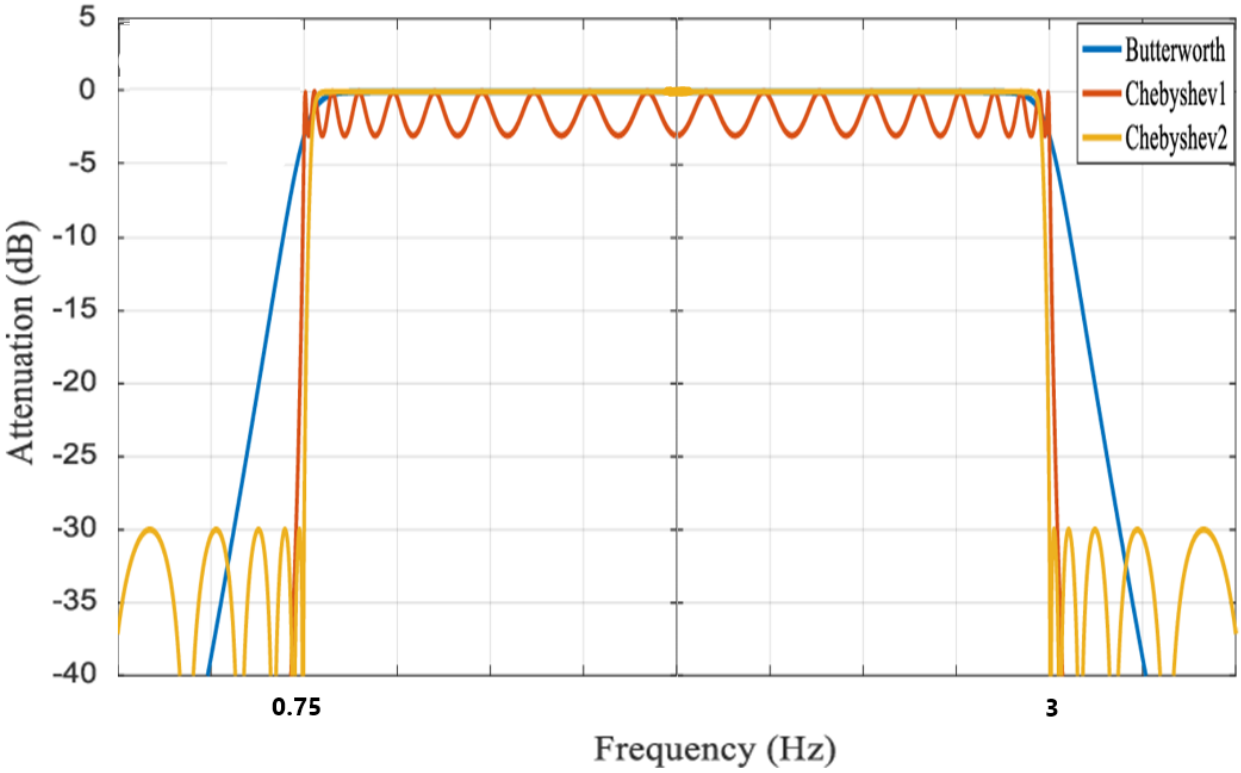

Figure 16: The frequency response of the Chebyshev and the Butterworth bandpass filters. The cut-off frequencies are depicted here at 0.75 and 3 Hz. Adapted from: [72]

2.4.2 Chebyshev Filters

Chebyshev filters represent another type of filter frequently utilized in rPPG research. They offer a steeper roll-off in the stopband compared to the Butterworth filter, albeit at the expense of introducing ripples in either the passband (Type 1) or the stopband (Type 2), as illustrated in Figure 16 [73]. Specifically, the Chebyshev Type 2 filter exhibits ripples in the stopband, facilitating faster attenuation of frequencies in that region compared to the Butterworth filter. This characteristic renders the Chebyshev Type 2 filter particularly advantageous for rPPG applications, as it allows for efficient attenuation of unwanted frequencies outside the cut-off frequency while minimizing attenuation of the signal of interest within the passband.

2.4.3 Pre-processing

In the pre-processing stage of the application, a moving average filter is employed. This filter operates by considering a window of frames over a specified timespan, continuously shifting with the addition of each new frame [56]. The moving average filter is renowned for its

ability to smooth the signal and capture its general trend. By applying this filter, abrupt motion artefacts noise can be mitigated, and high-frequency noise as well as intermittent motion artefacts can be effectively suppressed [56]. Overall, the moving average filter plays a crucial role in enhancing the quality of the signal in rPPG applications by reducing noise and enhancing the clarity of physiological information.

3 Methods

3.1 Optimization of the rPPG Application

In an effort to optimize the functionality of the rPPG Application, a root cause analysis will be conducted. This analysis aims to identify and address potential bottlenecks that may impede the application's performance. Five key areas of concern have been identified and visualized in an association map, as depicted in Figure 17. These potential bottlenecks include:

1. **Camera** (Section 3.1.2): Issues related to the camera hardware or setup that may affect signal quality or data acquisition.
2. **Noise** (Section 3.1.3): Sources of noise within the signal, such as ambient noise or electronic interference, which can degrade signal clarity.
3. **Stability** (Section 3.1.4): Factors affecting the stability of the signal acquisition process, including fluctuations in lighting conditions or camera positioning.
4. **Motion Artefacts** (Section 3.1.3): Disturbances caused by subject movement or camera motion during signal acquisition, leading to artefacts in the data.
5. **Environment** (Section 3.1.3): External factors in the surrounding environment that may impact signal quality, such as ambient lighting or temperature.

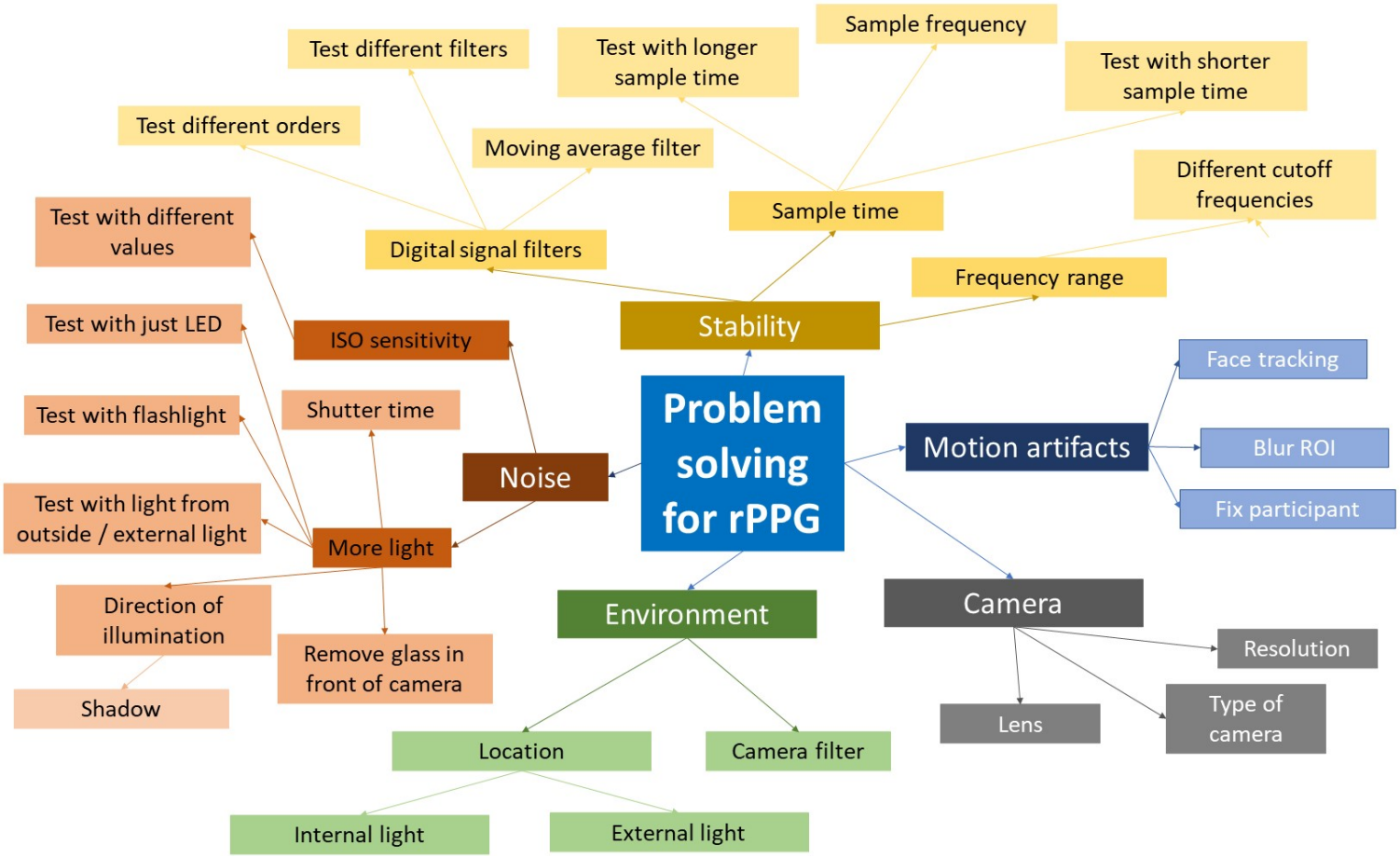

Figure 17: A mind-map for the optimization of the rPPG application.

3.1.1 The Testing Method

During the optimization process, a single test subject (the researcher) will be utilized under nearly identical conditions to ensure consistency. The test subject will be positioned in front of the camera for preliminary tests, maintaining a distance of approximately 0.5 meters between the camera and the subject. Each measurement session will last up to 30 seconds, during which the test subject will be instructed to maintain a steady posture and gaze directly at the camera. The experimental setup can be seen in Figure 18.

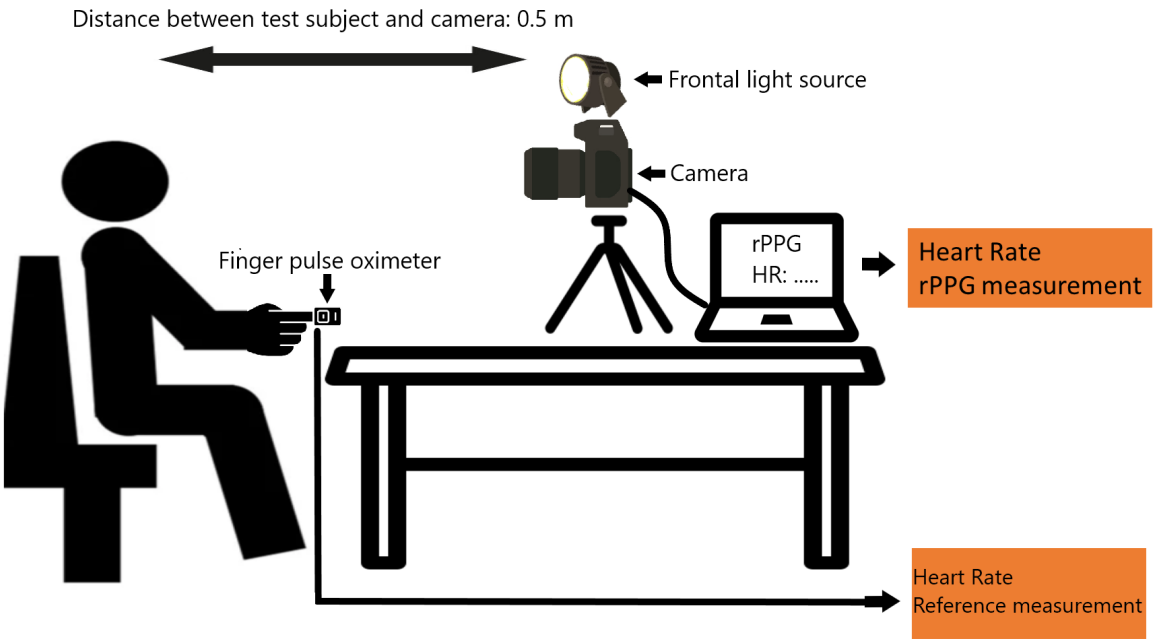

Figure 18: A schematic representation of the experimental setup.

To ensure robustness, each measurement will be repeated five times to account for variability. The POS rPPG method will be employed during the preliminary testing phase, as it is considered the state-of-the-art method according to existing literature.

Various parameters for both the camera and the application will be systematically tested and adjusted as needed. Additionally, different cameras and light sources will be evaluated to determine their impact on signal quality and performance. Through this rigorous testing process, optimal settings and configurations will be identified to enhance the accuracy and reliability of the rPPG application.

3.1.2 Camera

In this research, several cameras are utilized for data acquisition, each serving specific purposes. The cameras employed include:

1. **Sony a6000 and HP Webcam**: These cameras are used for ambient measurements. The Sony a6000 (1920 x 1080 pixels) is a high-quality digital camera, while the HP webcam (640×480 pixels) serves as a more affordable option.

2. **HQCAM NIR Camera**: The HQCAM NIR camera is a 1920×1080 pixel camera equipped with a built-in ring of 940 nm NIR-LEDs. It is commonly used for surveillance purposes in low-light conditions and captures 30 frames per second.

3. **Near-Infrared Modified Sony NEX-5T**: This camera has been modified for near-infrared imaging, enhancing its sensitivity to NIR wavelengths. A NIR spotlight (centre

wavelength at 850 nm) was used for the NIR illumination during the NIR measurements with the Sony NEX-5T (1920×1080 pixels, 60 fps).

The Sony cameras (a6000 and NEX-5T) are connected to the PC via a video capture card, resulting in a maximum resolution of 2MP HD (1980 x 1080). Both Sony cameras can achieve a frame rate of up to 60 fps, while the HQCAM NIR camera and the HP webcam operate at 30 fps The HQCAM NIR camera is connected to the PC through an USB cable.

The HQCAM NIR camera is of particular interest due to its affordability and built-in NIR-LEDs. It features a NIR filter with a passband ranging from 800 to 1064 nm, making it suitable for capturing near-infrared signals.

3.1.3 Noise, Motion Artefacts and the Environment

To mitigate noise interference, we will manipulate the lighting conditions during testing on the test subject. Three distinct lighting conditions will be employed:

1. **Darkness with HQCAM NIR-LEDs Only**: In this condition, the test subject will be positioned in darkness, with illumination provided solely by the NIR-LEDs integrated into the HQCAM camera.

2. **Darkness with Additional NIR Flashlight**: Similar to the first condition, the test subject will be in darkness, but with supplementary illumination from a NIR flashlight in addition to the NIR-LEDs of the HQCAM camera.

3. **Natural and NIR-LED Illumination**: In this condition, the test subject will be exposed to ambient sunlight along with illumination from the built-in NIR-LEDs of the HQCAM camera.

By varying the lighting conditions in this manner, we aim to evaluate the impact of different lighting sources on noise levels in the acquired signals. This comprehensive approach will provide insights into the effectiveness of each lighting configuration in reducing noise and enhancing signal quality during rPPG measurements.

In addition to manipulating lighting conditions, we will also vary the gain level of the camera to assess its impact on noise levels. The gain levels selected for experimentation include 1, 3, 5, 7, and 8. These varying gain levels will be applied while ensuring that the exposure is adjusted accordingly to maintain brightness levels within the optimal range of 100 to 150, as reported in the literature [66]. Given that the ISO sensitivity of the HQCAM camera cannot be adjusted, tests related to ISO sensitivity adjustments will not be conducted. Instead, focus will be placed on evaluating the influence of different gain levels on noise levels during rPPG measurements. By systematically varying the gain levels while controlling other parameters, we aim to elucidate the optimal gain setting that minimizes noise and enhances signal quality in our experimental setup.

To comprehensively assess the impact of illumination direction on rPPG measurements, the following setups will be employed with respect to the direction of sunlight:

1. **Directly Facing Window**: The test subject will be positioned directly facing a window, receiving direct sunlight as the a source of illumination.

2. **20 Degrees from Window**: In this setup, the test subject will be seated at a 20-degree angle relative to the window, allowing sunlight to illuminate the subject's face from an oblique angle.

3. **45 Degrees from Window**: In this setup, the test subject will be seated at a 45-degree angle relative to the window, allowing sunlight to illuminate the subject's face from an oblique angle.

4. **90 Degrees from Window**: The test subject will be positioned perpendicular to the window, receiving sunlight from the side.

By varying the direction of sunlight illumination in this manner, we aim to investigate how different lighting angles affect the quality of rPPG signals. The uneven surface of the face may result in varying levels of brightness and shadow, potentially impacting the reliability of rPPG measurements [15]. This comprehensive approach will provide insights into the optimal positioning of subjects relative to sunlight sources during rPPG data acquisition.

To evaluate the influence of motion artefacts on rPPG measurements, tests will be conducted under varying conditions:

1. **Free Head Movement**: In this condition, the test subject will be instructed to remain seated without any constraints on head movement. They will be free to move their head naturally during the measurement process.

2. **Head Resting on Headrest**: For this setup, the test subject will be provided with a headrest to stabilize their head during the measurement. The headrest will ensure minimal head movement during the data acquisition process.

By conducting measurements under these different conditions, we aim to assess how motion artefacts impact the quality and reliability of rPPG signals. Stabilizing the head with a headrest may help minimize motion artefacts, thereby improving the accuracy of rPPG measurements. Comparing results obtained under free head movement and headrest conditions will provide valuable insights into the effectiveness of motion artefact mitigation of our rPPG application.

3.1.4 Stability

In the optimization process, various configurations of signal filters and parameters will be tested to enhance the quality of rPPG signals:

- **Butterworth and Chebyshev Type 2 Bandpass Filters**: Filters will be tested at different orders (2, 4, 6, and 8) to assess their effectiveness in attenuating noise and preserving relevant signal components. Both Butterworth and Chebyshev Type 2 filters will be evaluated to compare their performance characteristics.

- **Moving Average Filter**: Different window sizes for the moving average filter will be tested to evaluate their impact on signal smoothing and noise reduction. The moving average filter's ability to mitigate abrupt motion artefacts and high-frequency noise will be assessed across various window sizes.
- **Frequency Ranges for Bandpass Filters**: Different frequency ranges will be examined for the bandpass filters to identify the optimal range for capturing physiological signal components while suppressing noise and artefacts effectively.
- **Frame Rate (FPS) Considerations**: Due to limitations in adjusting the FPS of the HQCAM camera, the sample frequency cannot be modified. Therefore, the impact of fixed FPS on signal quality will be noted and considered in the analysis of experimental results.

By systematically testing these configurations and parameters, we aim to identify the most suitable settings for the signal filters and optimize the rPPG application's performance under different conditions and scenarios.

3.2 Experiment with Test Subjects

3.2.1 Experimental Setup and Measurement Equipment

In this section, the experiment with different human test subjects will be detailed. These measurements will be conducted after the optimization process, the results of the optimization process will be implemented. The experimental setup, as illustrated in Figure 18, includes the following components:

- **Cameras**:
  - **Sony a6000**: This camera has a maximum frame rate of 60 fps, making it suitable for measurements in ambient conditions.
  - **HQCAM**: Equipped with a maximum frame rate of 30 fps and 2MP HD 1980 x 1080 resolution, this camera will be utilized for the NIR measurements.
- **Connection to PC**: The Sony a6000 camera will be connected to a PC via a USB HD Video Capture Device. Video images from this camera will be captured at 2MP HD 1980 X 1080 resolution.
- **Finger Pulse Oximeter:** A SPO55 finger pulse oximeter from SilverCrest Health-ForYou will be utilized to measure the heart rate simultaneously with the camera measurements. The SPO55 oximeter offers an accuracy of $\pm$ 2 beats per minute [74].
- Other parameters and choices for the rPPG application can be seen in Table 6 in the results section.

This setup enables the simultaneous capture of video data using the rPPG application, along with the measurement of the subject's heart rate using the finger pulse oximeter. These reference measurements will facilitate comparison and validation of the camera-based measurements.

3.2.2 Experimental Protocol

In this experiment, the camera was positioned at a distance of 0.5 meters from the test subject, following the methodology established by Verkruysse et al. [62]. The test subject was instructed to gaze directly at the camera, and their head was placed on a headrest to minimize motion artefacts. The camera's height and orientation were adjusted to ensure that the entire face of the participant was captured within the frame. During the NIR measurements, the subject's face was illuminated from the front by the built-in 940 nm LEDs for the HQCAM camera.

A total of eighteen test subjects participated in this experiment, with their distribution across different skin types outlined in Table 1. Prior to participation, written consent was obtained from each volunteer, and the experimental procedures were approved by the ethics committee of the University of Twente (application nr. 230114).

Skin Type	I	II	III	IV	V	VI
Amount of Participants	3	5	3	2	1	4

Table 1: The distribution of the participants based on skin types.

3.2.3 Measurement Protocol

The measurements were taken according to the following protocol:

1. The participant is seated in front of the camera.
2. A finger pulse oximeter is placed on the finger of the participant to measure the reference heart rate.
3. The ambient / NIR light source frontally illuminates the face of the participant.
4. The measurement will take thirty seconds.
5. Steps 2 to 4 will be repeated in ambient and NIR conditions.
6. The participant will be asked to walk up and down two flights of stairs to elevate their heart rate. This enables us to see the rPPG algorithms' functioning in different heart zones.
7. Steps 2 to 4 will again be repeated in ambient and NIR conditions.
8. Ten measurements will be taken per test subject (5 ambient, 5 NIR).

3.2.4 Analysis and Statistics

3.2.4.1 Heart Rate Error

The evaluation metrics used in this study are the mean percentage error (MPE, from here on forward referred to as heart rate error (HRE)) and the signal-to-noise ratio (SNR). The correspondence between the heart rate extracted from the rPPG pulse signal by the algorithms and the pulse rate extracted by the finger pulse oximeter is evaluated by the HRE. The HRE is defined as follows:

$$HRE = \frac{100}{N} \sum_{i=1}^{N} \frac{(HR_{\text{Algorithm}} - HR_{\text{ref}})}{HR_{\text{ref}}}. \tag{3.1}$$

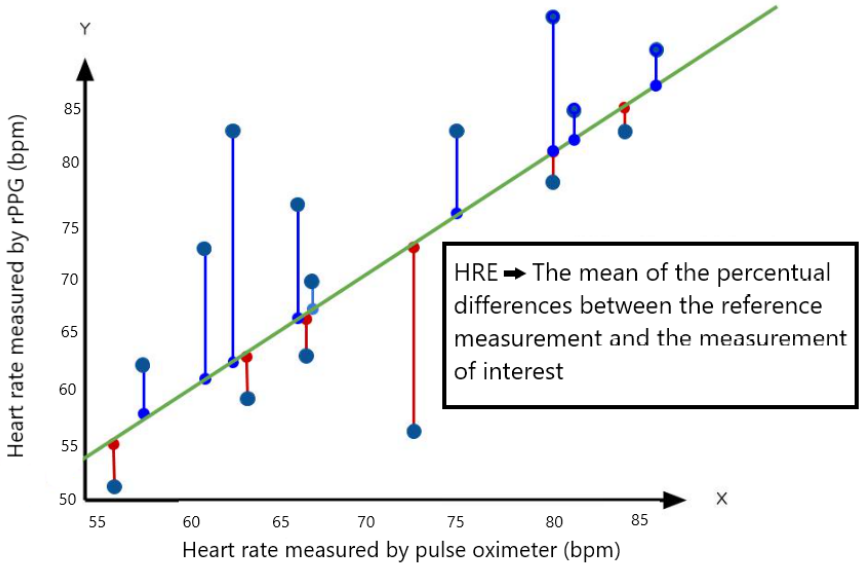

Figure 19: A visual representation of the mean absolute percentage error.

3.2.4.2 Signal-to-Noise Ratio

SNR analysis is used to obtain a quality metric from the signals produced during the experiments. The method used in this research project is adopted from de Haan et al. [45]. The ratio of the energy around the fundamental frequency plus the first harmonic of the pulse signal and the remaining energy contained in the spectrum is used in the calculation of the SNR metric. The first harmonic is also selected to account for harmonic distortion. The SNR is defined as follows:

$$SNR = 10log_{10}\left(\frac{\Sigma_{f=45}^{180}(U_{\mathrm{t}}(f)S(f))^2}{\Sigma_{f=45}^{180}((1-U_{\mathrm{t}}(f))S(f))^2}\right), \tag{3.2}$$

where U_t(f) is a template around the peak heart rate and its first harmonic detected by the finger pulse oximeter, and S(f) is the full frequency spectrum as measured by the algorithm. The template can be seen in Figure 20. The template around the peak heart rate and its first harmonic contain the five heart rates at either side to allow for heart rate variability [45].

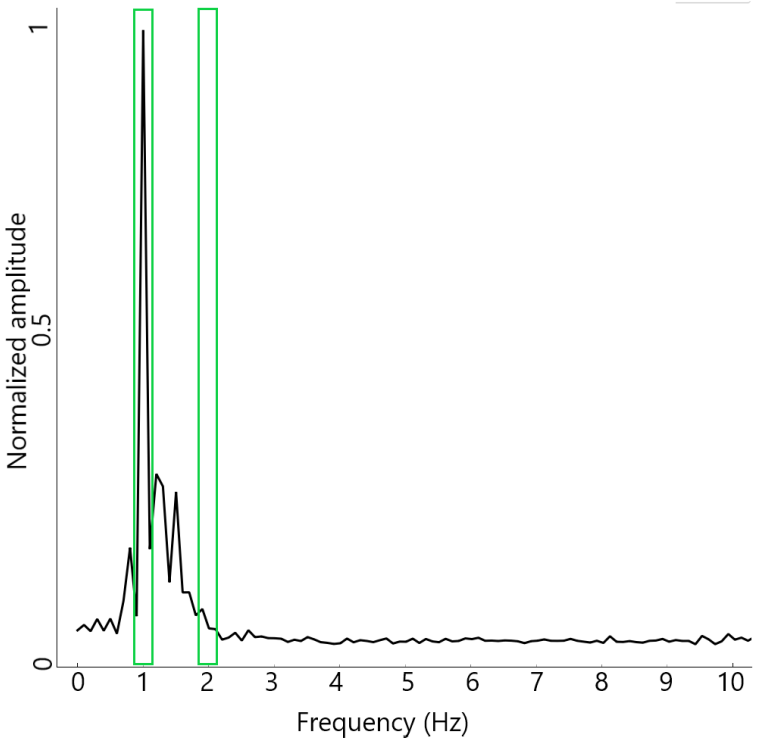

Figure 20: The template that is used in the SNR calculation. The template is centred around the heart rate frequency determined by the finger pulse oximeter and contains the five heart rates at either side to allow for heart rate variability. The first harmonic and the five heart rates at either side are also included in the template.

3.2.4.3 Analysis of Variance

Analysis of variance (ANOVA) is a statistical method used in research to assess the differences among group means in a data set [75]. The one-way ANOVA tests whether the group means of two or more groups are significantly different, using one independent variable. ANOVA aims to determine whether the observed variances between the groups are significant or if they could be attributed to random chance. The one-way ANOVA will be applied on the SNRa (average SNR) values to test the significance of differences between different measurement conditions. A common significance threshold is used in this thesis, $P < 0.05$. If the calculated p-value is smaller than 0.05, it indicates that there is a significant difference between the two groups.

3.3 The Flow of the rPPG Application

The application proposed in this thesis takes a stream of video as input. The input consists of a sequence of tuples of the form (frame[i], timestamp[i]), where i denotes the counter of video frames captured, frame[i] is a (width, height,3) matrix containing the RGB intensity values of each pixel and timestamp[i] denotes the time at which frame[i] was captured. The application pipeline can be seen in Figure 21.

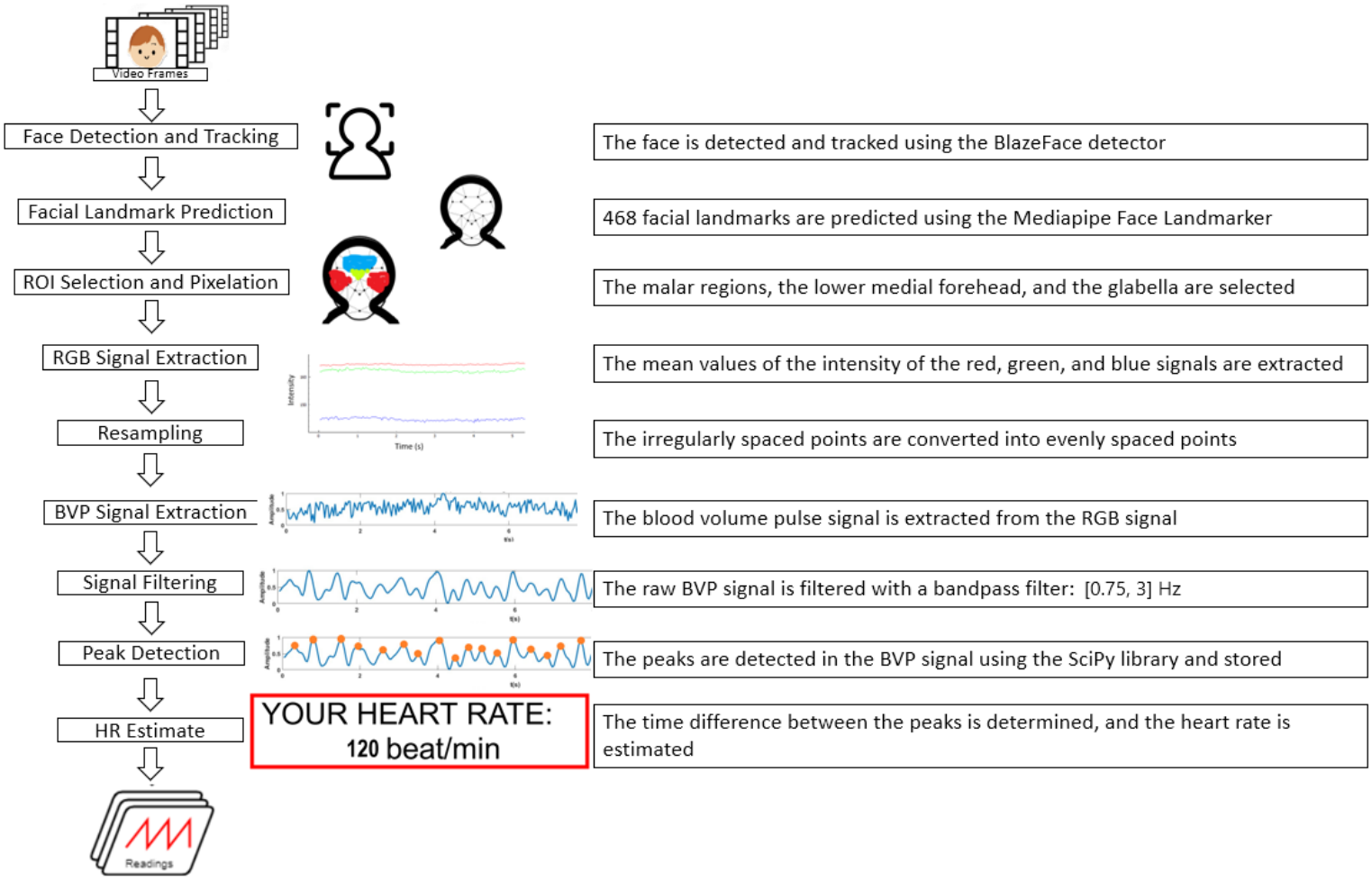

Figure 21: The flow of the rPPG application that is created in this thesis.

For every video frame (frame[i]), an average of the intensity of the RGB channels within a predicted skin ROI is computed and denoted as mean_rgb[i]. This process involves face detection (3.3.1), landmarks prediction (3.3.2), ROI selection (3.3.3) and RGB signal extraction (3.3.4). It is worth noting that aside from the initialization of the face and landmarks detection algorithm, no extra memory is required for these tasks.

Next, the blood volume pulse (BVP) signal will be estimated. The BVP signal is denoted as bvp[t] and collected from the raw RGB signal. Since the subsequent rPPG algorithms assume that the samples are evenly distributed in time, the asynchronous raw RGB signal is

resampled to ensure uniform timing. Then, we utilize one of the rPPG methods, explained in Section 2.2.4, to convert the skin RGB signal into the BVP signal. To clean the signal for peak detection, a bandpass filter is applied.

Lastly, the heart rate is estimated using the filtered BVP signal. The first step involves applying peak detection on the BVP signal to identify the true heartbeats; from this, the pulse-to-pulse intervals can be calculated. Estimations can be made about the heart rate by analysing the pulse-to-pulse intervals. In the subsequent sections, we will outline the sequential flow of the application. We will detail each step, discussing its purpose and function in the overall process.

3.3.1 Face Detection

For face detection, both the OpenCV computer vision and machine learning library as well as the MediaPipe face detection machine learning model are integrated into the application [76][77]. Both of these libraries are openly accessible. The MediaPipe method functioned more smoothly with the application, so the decision was made to make this the primary method. The MediaPipe method makes use of the BlazeFace face detector. BlazeFace, a machine learning model (a kind of AI), has an average accuracy of 98.61% and has been trained on a database of 66,000 videos [78]. BlazeFace, has an average CPU latency of 2.61 ms which is short enough to detect the face in every frame at 60 fps [79]. The process generates a rectangle representing the detected face in the format (x_{ul}, y_{ul}, width, height), where ul denotes the rectangle's upper left corner around the detected face. For our application, only one face is detected at a time, whereas BlazeFace can detect up to 10 faces at a time.

Input: frame[i]
Output: rect[i]

3.3.2 Landmarks Prediction

The landmarks are detected using the Mediapipe Face Landmarker; it uses machine learning models that can work with single images or a continuous stream of images. The model takes a frame and a rectangle corresponding to the detected face area as input and generates the output shape[i]. The shape[i] represents a 468-point list containing the pixel coordinates of the 468 facial landmarks modelled by this machine learning instance [52]. The 468 landmarks are visualized in Figure 22.

Input: frame[i], rect[i]
Output: shape[i]

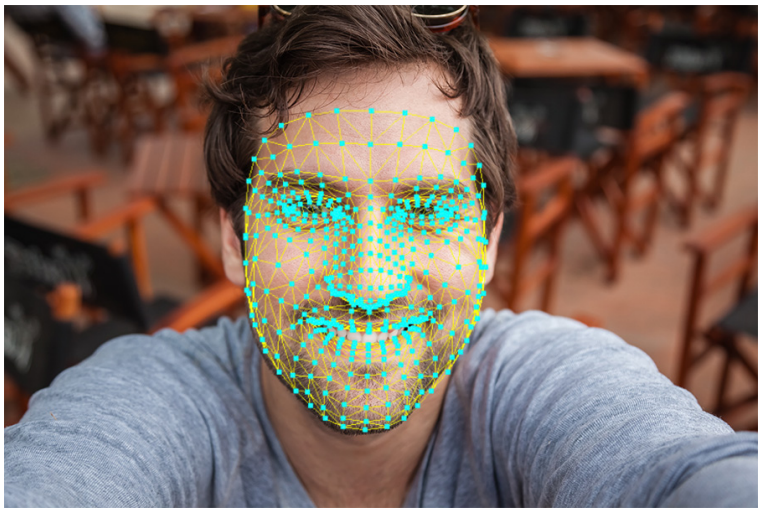

Figure 22: A graphic representation of the 468 facial landmarks that are detected by the Mediapipe Face Landmarker. Source: [80]

3.3.3 ROI Selection

Selecting the Region of Interest (ROI) involves utilizing the predicted landmarks to create contours around the relevant regions. In this research, we focus on targeting areas in the face; in later research, other body areas should also be targeted. The information the camera receives differs per area of the face being targeted. The main reason for this difference is the thickness of the skin; the thicker the skin, the deeper the blood vessels are situated respectively [55]. According to Dae-Yael et al., the facial regions best suited for rPPG signal extraction are the malar regions, the lower medial forehead and the glabella [56]. The corresponding pixel coordinates were used to enclose the ROI; see Figure 23. The skin close to the eyes, mouth and nose has been excluded from the ROI since these areas often move.

Figure 23: The ROI depicted on a face in NIR, contouring the malar regions, the lower medial forehead and the glabella.

The selection of the ROI is a critical step for the rPPG analysis. It is crucial to avoid noise from non-skin areas during sampling, as this can interfere with the detection of the delicate rPPG signal. The output, mask[i], is a binary matrix of dimensions (width, height), containing ones for skin areas and zeros for non-skin areas.

Input: shape[i]
Output: mask[i]

3.3.4 RGB Signal Extraction

The obtained skin mask is used to mask the corresponding frame using a bitwise operation, resulting in a new masked_frame[i]. From this masked_frame[i], the red, green and blue intensities of the pixels are extracted over the ROI. These intensities are averaged and denoted in a (3,1) vector as mean_rgb[i]. This vector is computed by summing the masked_frame's RGB intensities of the masked_frame[i] over its width and height, and then dividing the sum by the total number of skin pixels in the mask[i].

Input: frame[i], mask[i]
Output: mean_rgb[i]

3.3.5 Resampling

In real-time video processing, the video signal is often processed asynchronously. This means that the sampled video frames are not evenly temporally spaced. This asynchronicity can be attributed to the fact that the entire rPPG pipeline, including video capture and processing, runs on a single computer thread. Consequently, the processing of each new video frame takes a varying amount of time, and only when the current frame is processed a new frame is grabbed. This leads to an irregular temporal sampling pattern.

For efficient signal processing in the subsequent stages of the pipeline, it is essential to have a fixed sampling rate. So, by adding a resampling step to the pipeline, we can generate an evenly-spaced signal for further processing. This entails converting the irregularly spaced points in time into evenly spaced points. The resampling process uses linear interpolation; each pair of consecutive frames generates evenly spaced points using the sampling frequency (f_s). The evenly spaced time points are stored in a 1D array-like list ts.

Input: frame[i], frame[i + 1]
Output: ts

3.3.6 BVP Signal Extraction and Filtering

Using a rPPG algorithm, a one-dimensional BVP signal can be extracted from the RGB signal. The rPPG algorithms GREEN, NIR, CHROM and POS from Section 2.2.4 have been implemented in the application.

The BVP signal from the rPPG algorithms has been through a moving average filter, which smoothed and cleaned the signal using the data points in a window of 300 frames, for the 30

fps cameras this is a time frame of 10 seconds. The BVP signal will be filtered because this simplifies finding the true pulse peaks in the BVP signal. The signal can be filtered using the SciPy library, from which both the Butterworth and the Cheby2 bandpass filters have been implemented. The bandpass filter range has been set at [0.75, 3] Hz since these frequencies correspond to a heart rate range of 45 to 180 beats per minute. The output after the filters is a 1D array-like list vs containing the filtered BVP signal.

Input: mean_rgb[i], ts
Output: vs

3.3.7 Peak Detection

The SciPy library is useful for detecting peaks in a 1D array with the scipy.signal.find_peaks function. This function takes our vs 1D-array with the filtered BVP signal and starts detecting peaks. However, we first need to define which peaks it needs to detect because the function considers everything a peak if it is higher than its neighbour on either side. As you would expect, this is problematic with a noisy signal.

To filter the list of peaks that the SciPy function initially produces, we can give the function a minimum distance between the peaks and a minimum height. The minimum distance between the peaks is set to 0.33 * the sampling rate. The 0.33 value corresponds to 0.33 seconds, which is the time between heartbeats at a frequency of 181 beats per minute. Applying these settings to the list of peaks gives us a list with the indices between the true heartbeats.

Input: vs, ts
Output: indices, ts

3.3.8 HR Estimate

The indices with the true heartbeats get paired with the corresponding timestamps. The average of the differences between the indices is taken; this gives us a heartbeat in Hertz, see Equation 3.3.

$$HR_{Hertz} = mean(diff(ts[indices])) \tag{3.3}$$

When we multiply 60 by the outcome of Equation 3.3, we get the HR in beats per minute (bpm); see Equation 3.4.

$$HR_{bmp} = 60 * HR_{Hertz} \tag{3.4}$$

Now that we have the HR in bpm, we can take the average of the last three calculated heart rates and the last calculated average to filter out any sudden drops or rises in the calculated heart rate that are not continuous. The weighting of the average heart rate can be seen in Equation 3.5.

$$HR_{bpm}shown = (3 * (HR_{bpm}[fromthelastthreeframes]) + 2 * HR_{bpm})/5 \tag{3.5}$$

Input: indices, ts
Output: HR_{bpm}shown

3.3.9 Signal Quality Index

To assess the quality of the rPPG signal, we will employ a signal quality index (SQI). Skewness, which reflects the asymmetry of the probability distribution, is often linked to corrupted rPPG signals [81]. Eldengi et al. have suggested that skewness SQI is the most effective index for evaluating PPG signals [82]. To calculate skewness, we will utilize the skew function from the SciPy library.

3.4 Data Processing and Interpretation

For a clearer understanding of how results are obtained from the rPPG application, a schematic representation of the process is depicted in Figure 24. The process commences with the retrieval of the raw BVP signal from the POS algorithm. This BVP signal undergoes filtration through both a Bandpass Filter and a moving average filter (Section 3.3.6). Subsequently, peaks in the filtered BVP signal are detected, and the signal is Fourier transformed to facilitate heart rate determination (Section 3.3.7).

During a measurement with the rPPG application, a heart rate value is outputted into the Command Prompt every three seconds. Each heart rate value is accompanied by an SQI value. Seven consecutive heart rate values with satisfactory SQI values (between -5 and 5) are considered a measurement. These seven heart rate values are then averaged and incorporated into the data processing procedure. The resultant average value is compared with the heart rate value obtained from the finger pulse oximeter.

Interpretation of the HRE values is based on comparable research in literature, as outlined in references [66], [83], and [84]. Table 2 provides interpretations of the HRE values.

HRE value (%)	Interpretation	Color
$x \leq 3$	Good	Green
$3 < x < 5$	Okay	Orange
$x \geq 5$	Bad	Red

Table 2: Interpretation of the HRE values

The template from Figure 20 is used in the calculation of the SNR value. The interpretation of the SNR values is based on SNR values that have been achieved in comparable research in literature [45][60][83]. The interpretation of the SNR values can be seen in Table 3:

SNR values (dB)	Interpretation	Color
$x \geq 7$	Good	Green
$5 < x < 7$	Okay	Orange
$x \leq 5$	Bad	Red

Table 3: Interpretation of the SNR values

The color indications will be used in the bar charts in the results section to give an indication of the value of the evaluation metrics.

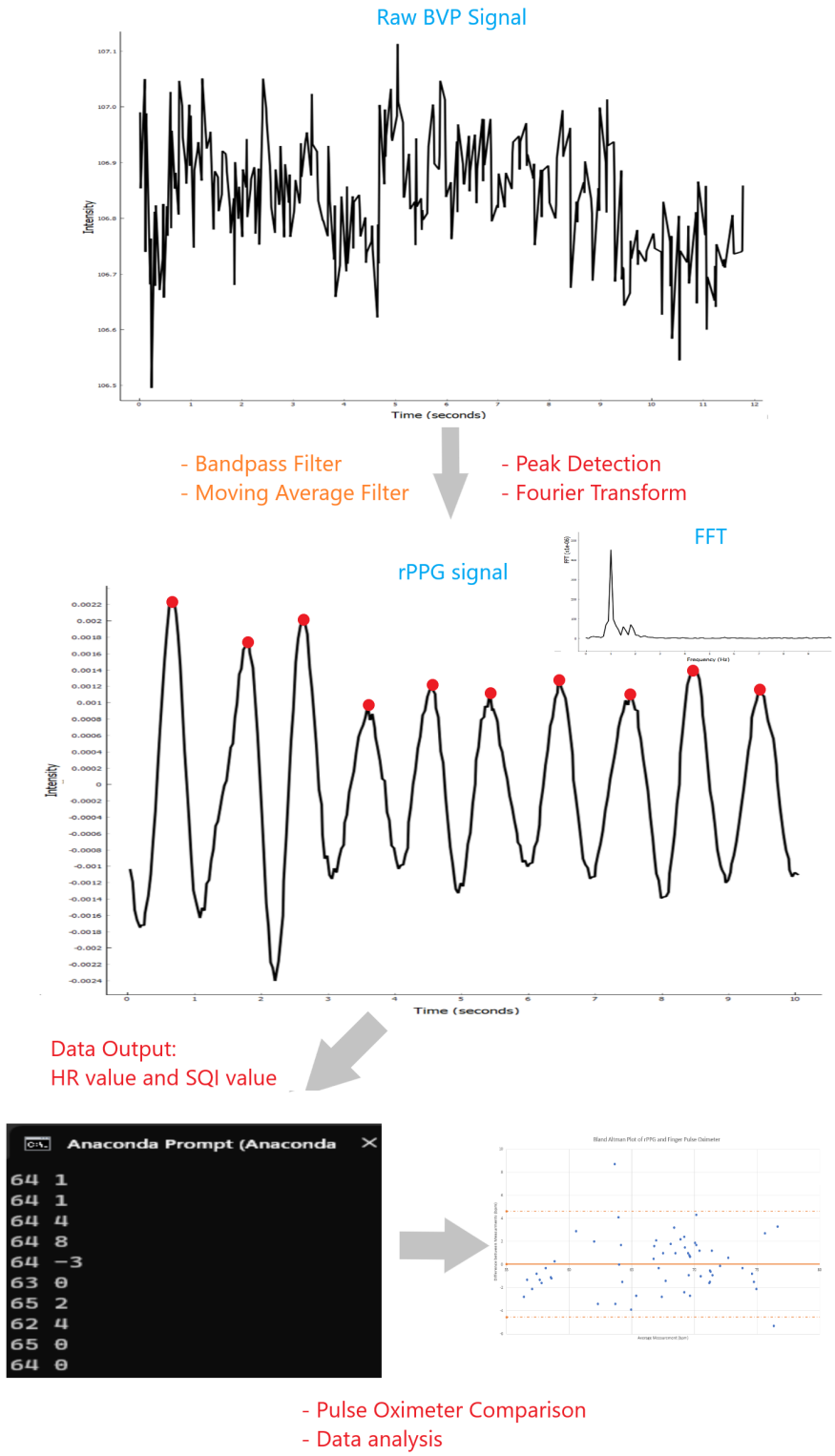

Figure 24: A schematic overview of the process of retrieving results from the rPPG application, starting with raw BVP signal and ending with data figures.

4 Results

4.1 Results of Tests with Human Subjects with varying Skin Types

Figures 25 and 26 depict boxplots illustrating the distribution of HRE values for rPPG measurements conducted under ambient and NIR (940 nm) conditions across different skin types. Analyzing Figure 25, it becomes apparent that HRE values for skin type VI exhibit considerable variability (-15% to 20%) under ambient conditions compared to other skin type categories. Conversely, HRE values for skin types I - II and III - IV - V remain relatively consistent within the range of -5% to 5%.

Turning to Figure 26, the data suggests that NIR rPPG yields improved HRE values for skin type VI in comparison to ambient rPPG. Additionally, the HRE values for skin types I - II and III - IV - V exhibit slightly greater variability compared to those obtained under ambient conditions.

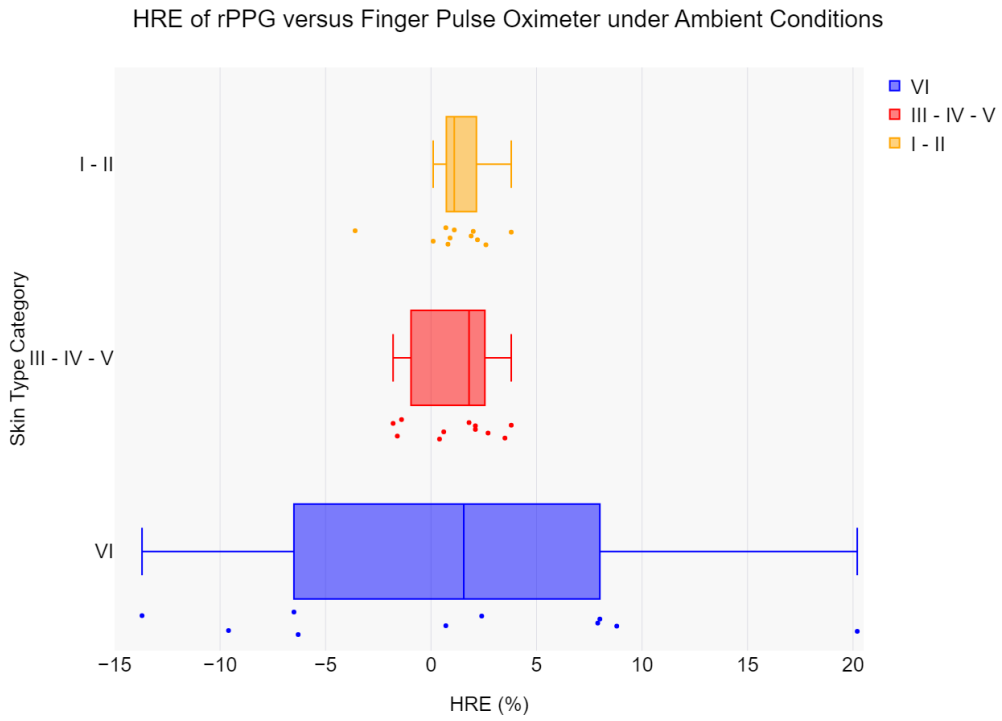

Figure 25: The evaluation metric HRE of the rPPG measurement with the Sony a6000 and the finger pulse oximeter under ambient conditions, where the x-axis and y-axis denote the skin type and the HRE, respectively.

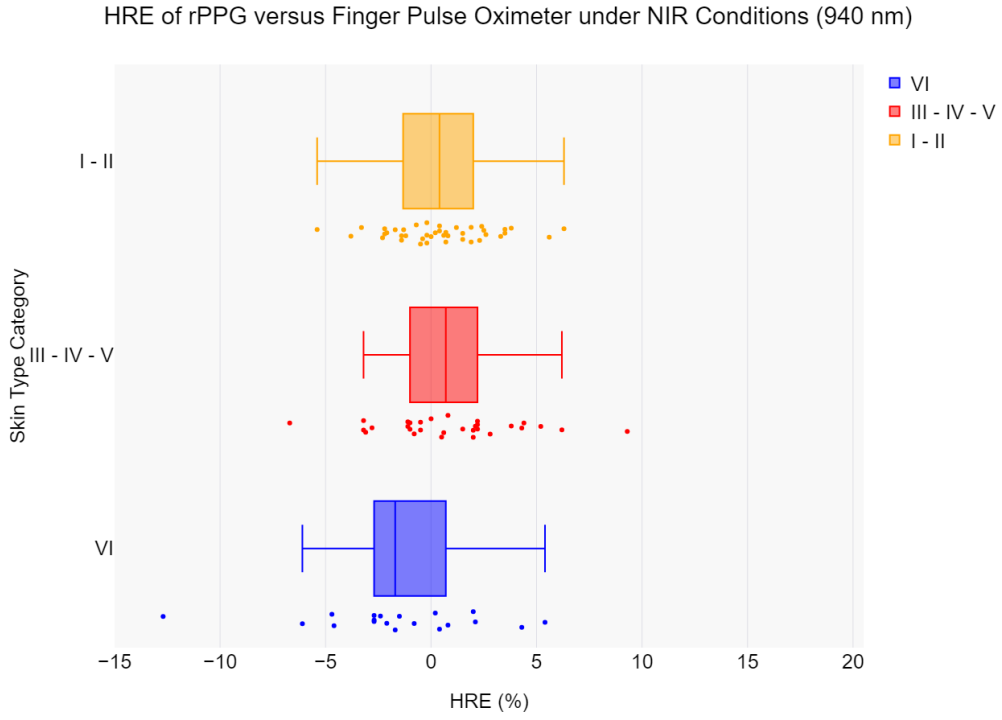

Figure 26: The evaluation metric HRE of the rPPG measurement with the HQCAM (940 nm) and the finger pulse oximeter under NIR conditions, where the x-axis and y-axis denote the skin type and the HRE, respectively.

In Figure 27, the SNR evaluation metric for rPPG measurements conducted under both ambient and NIR (940 nm) conditions is presented. It is evident that under ambient conditions, the SNR value for skin type VI is notably low. However, under NIR conditions, the SNR value for skin type VI demonstrates improvement and can be deemed acceptable. For skin type categories I - II and III - IV - V, the SNR values are high under ambient conditions, but slightly lower under NIR conditions, albeit still within acceptable ranges. The one-way ANOVA conducted between the skin type VI and the other two skin type groups yielded a p-value of $P < 0.001$ both times under ambient conditions, indicating a significant difference, see Table 4. In Table 5 the p-values between the skin type categories under NIR conditions can be seen, no significant differences were found.

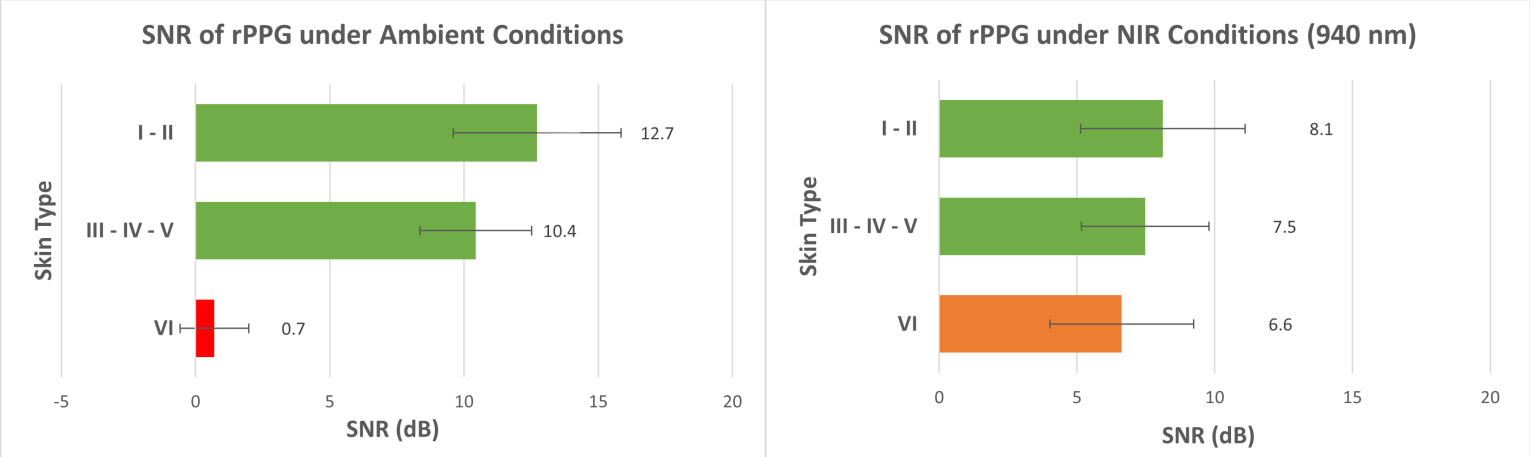

(a) The SNR metric of rPPG under ambient conditions for the different skin type categories.

(b) The SNR metric of rPPG under NIR (940 nm) conditions for the different skin type categories.

Figure 27: The SNR metric of rPPG under ambient and NIR (940 nm) conditions for the different skin type categories.

Ambient	I - II	III - IV - V	VI
I - II	-	P = .29	**P < .001**
III - IV - V	P = .29	-	**P < .001**
VI	**P < .001**	**P < .001**	-

Table 4: The p-values for the one-way ANOVA of the SNRa values of the rPPG measurements under ambient conditions between the skin type categories.

NIR (940 nm)	I - II	III - IV - V	VI
I - II	-	P = .67	P = .12
III - IV - V	P = .67	-	P = .49
VI	P = .12	P = .49	-

Table 5: The p-values for the one-way ANOVA of the SNRa values of the rPPG measurements under NIR (940 nm) conditions between the skin type categories.

In Figure 28, a plot displaying the average HRE per measurement per test subject of the NIR rPPG (940 nm) and finger pulse oximeter measurements is presented. The 95% confidence interval spans from -6.1% to 6.2%.

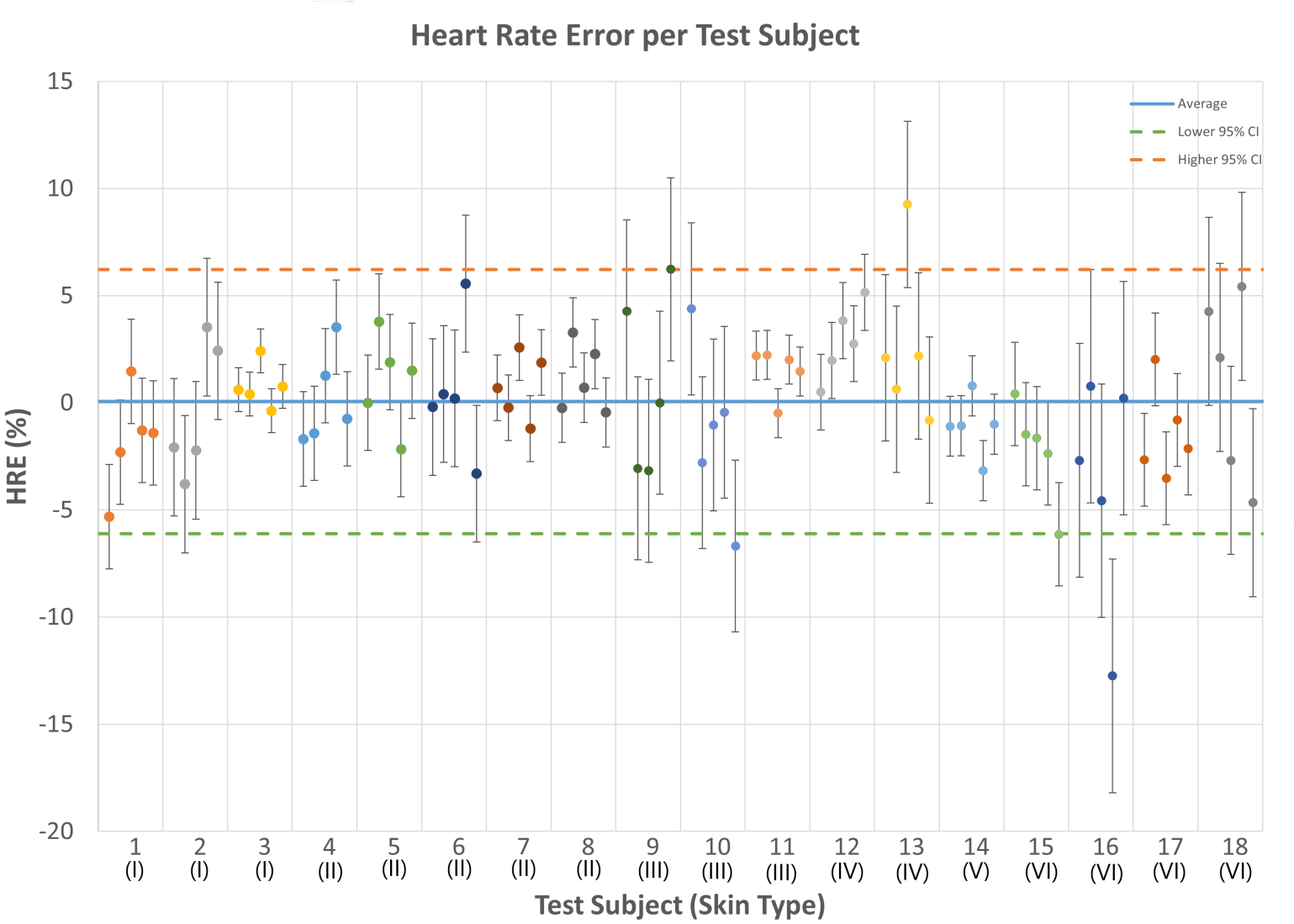

Figure 28: The HRE of the measurements per test subject for the NIR (940 nm) measurements.

In Figure 29, the plots depict the average HRE per test subject of the NIR rPPG (940 nm) and finger pulse oximeter measurements, divided per skin type group (I-II, III-IV-V, VI). The 95% confidence interval for skin type category I - II ranges from -4.2% to 4.7%, for skin type category III - IV - V from -5.4% to 7.3%, and for skin type VI from -9.4% to 6.1%.

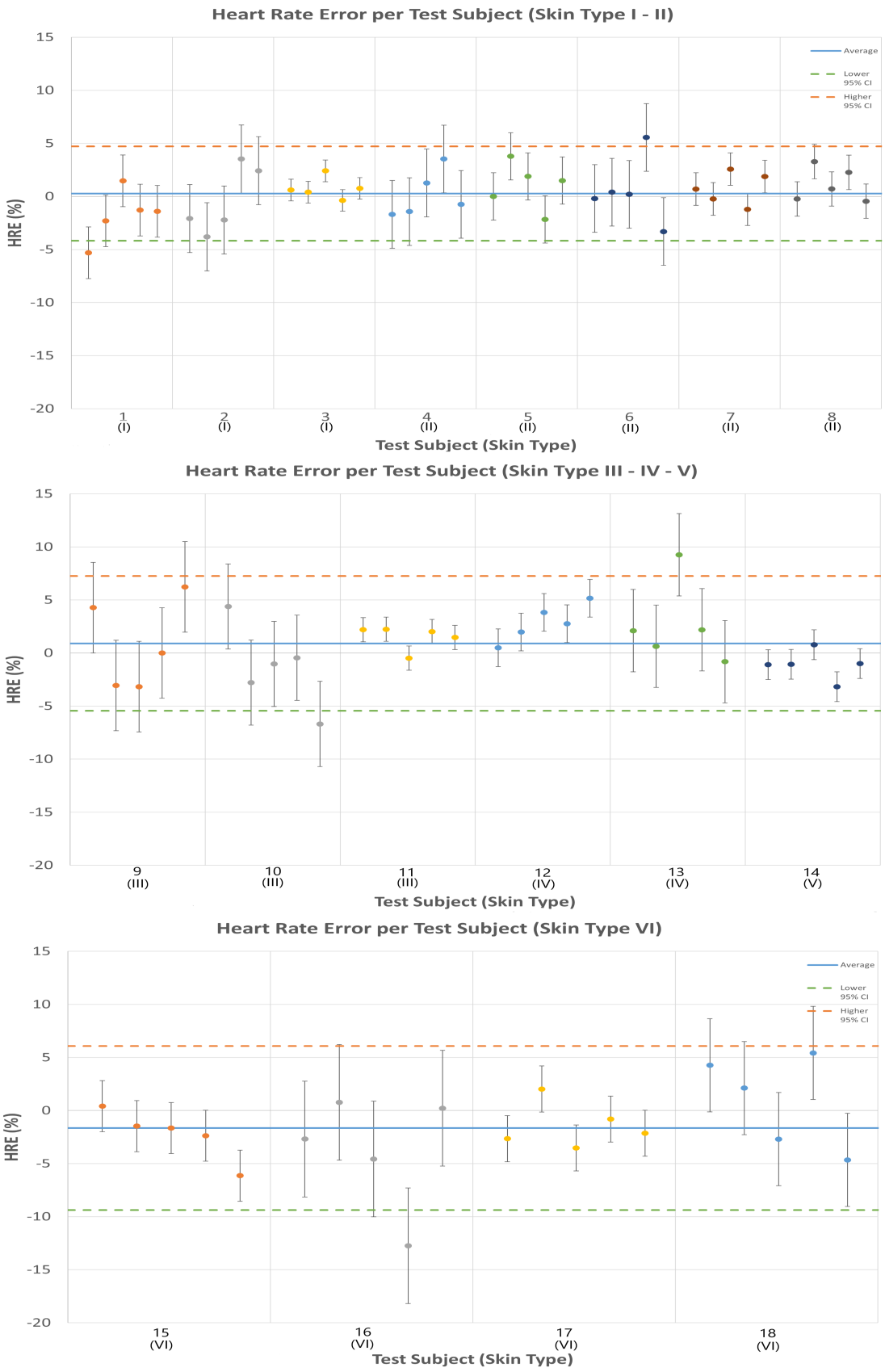

Figure 29: The HRE of the measurements per test subject for the NIR (940 nm) measurements divided per skin type group (I-II, III-IV-V, VI).

4.2 Results of the Optimization of the rPPG Application

In Table 6, the final settings and choices for the rPPG application are summarized. These settings and choices were utilized to collect the results presented in the preceding sections. For a more detailed examination of the optimization process results, please refer to Appendix 8.1.

Category	Selected Option
Camera	Ambient: Sony a6000 NIR: HQCAM
Angle of Illumination	0 degrees (head-on)
NIR Lighting	NIR-LEDs and outside light
Gain Level	Dependent on the illumination level
Head Fixation	Fixed head
Type and Order of Bandpass Filter	Type: Chebyshev Type 2 Order: 4
Frequency Range Bandpass Filter	45 - 180 Hz
Window Size of Moving Average Filter	10 seconds
rPPG Algorithm	POS

Table 6: The selected settings and choices for the rPPG application.

4.3 Application and Demonstrator Design

When the application is launched, two windows appear simultaneously. The first window is dedicated to rPPG functionalities, while the second window displays camera and video properties. The rPPG window comprises the following elements: the video feed, the calculated heart rate display, the logos of the University of Twente and the Techmed Centre, and a pushbutton. Figure 30 provides a visual representation of the rPPG window.

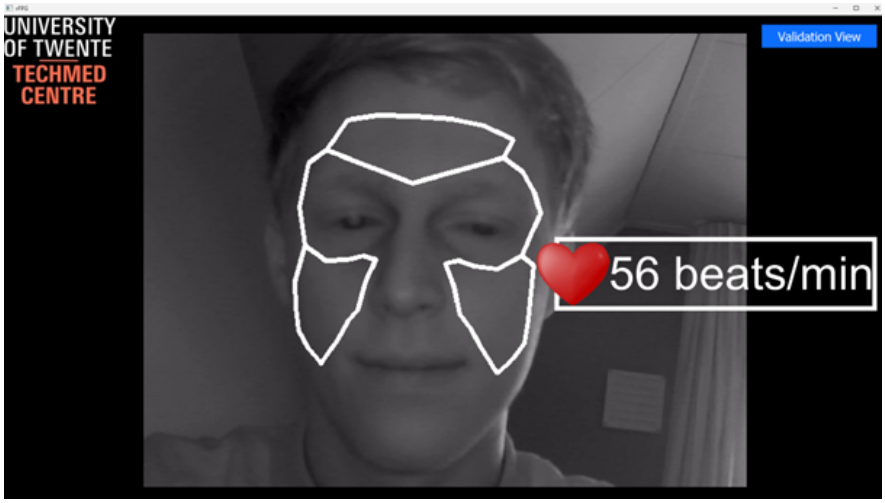

Figure 30: The main window of the rPPG application

In the camera and video properties window (Figure 31), users can fine-tune settings such as brightness, contrast, hue, saturation, sharpness, gamma, white balance, backlight compensation, gain, and exposure values.

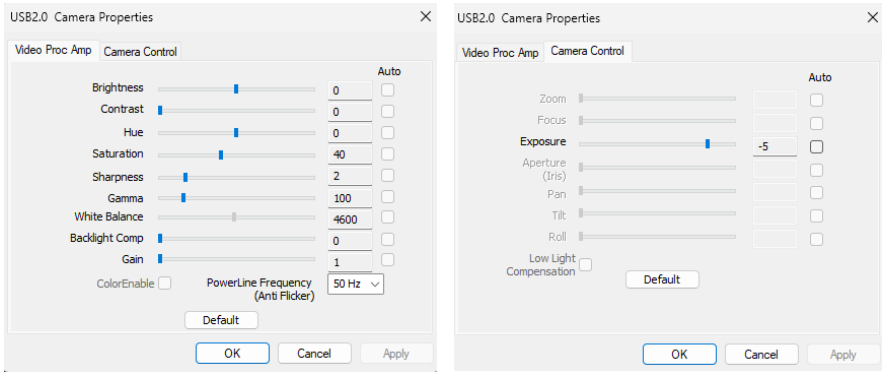

Figure 31: The camera properties windows

The pushbutton in the rPPG window leads the user to the validation window, depicted in Figure 32. The validation window includes two graphs, the calculated heart rate display, the SQI value, and two additional pushbuttons. The left graph in the validation window

illustrates the average brightness of the Region of Interest (ROI) in the video, which ideally falls within the range of 100 to 150, as recommended by Odinaev et al. [66]. On the other hand, the right graph in the validation window shows the Fourier transform of the rPPG signal. Additionally, by right-clicking the mouse, this graph can also display the rPPG signal itself. The SQI value serves as an indicator of the signal quality, with a value ranging from -5 to 5 signifying good signal quality.

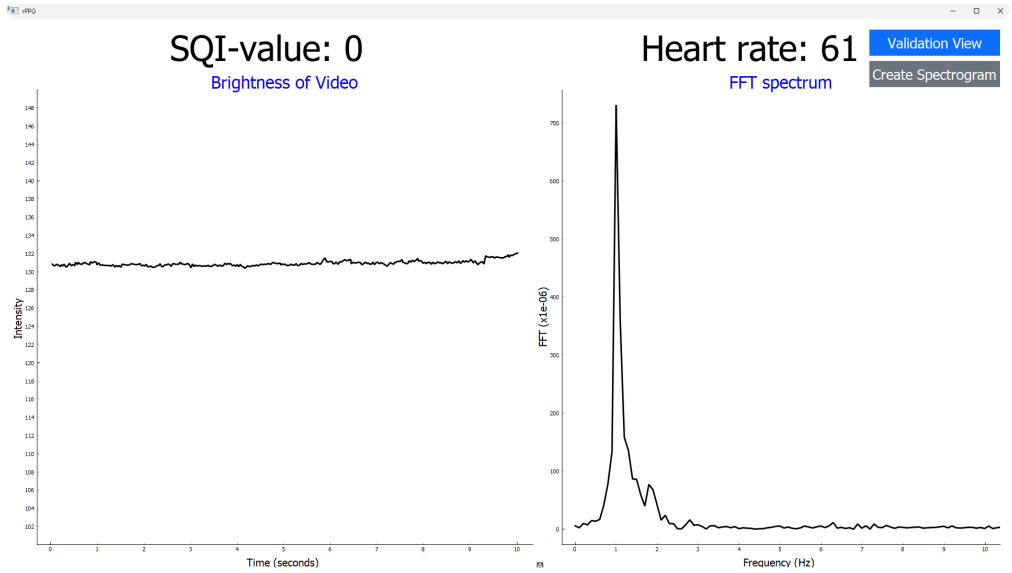

Figure 32: The validation window of the rPPG application.

When the "Create Spectrogram" pushbutton is activated, a new window displaying a spectrogram of the rPPG signal is generated, as illustrated in Figure 33. A spectrogram visually represents the spectrum of frequencies of the rPPG signal over time, providing valuable insights into its frequency components and variations.

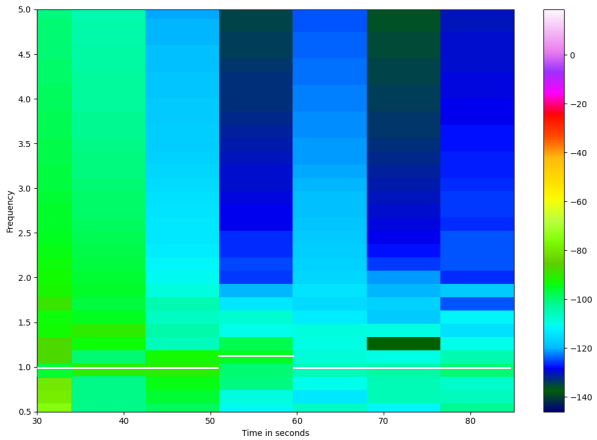

Figure 33: An example of a spectrogram created with the rPPG application. The white line indicates the highest frequency.

The setup of the demonstrator is depicted in Figure 34. The HQCAM can be conveniently positioned either on a laptop or a larger screen with a PC behind it, providing flexibility in the demonstration setup.

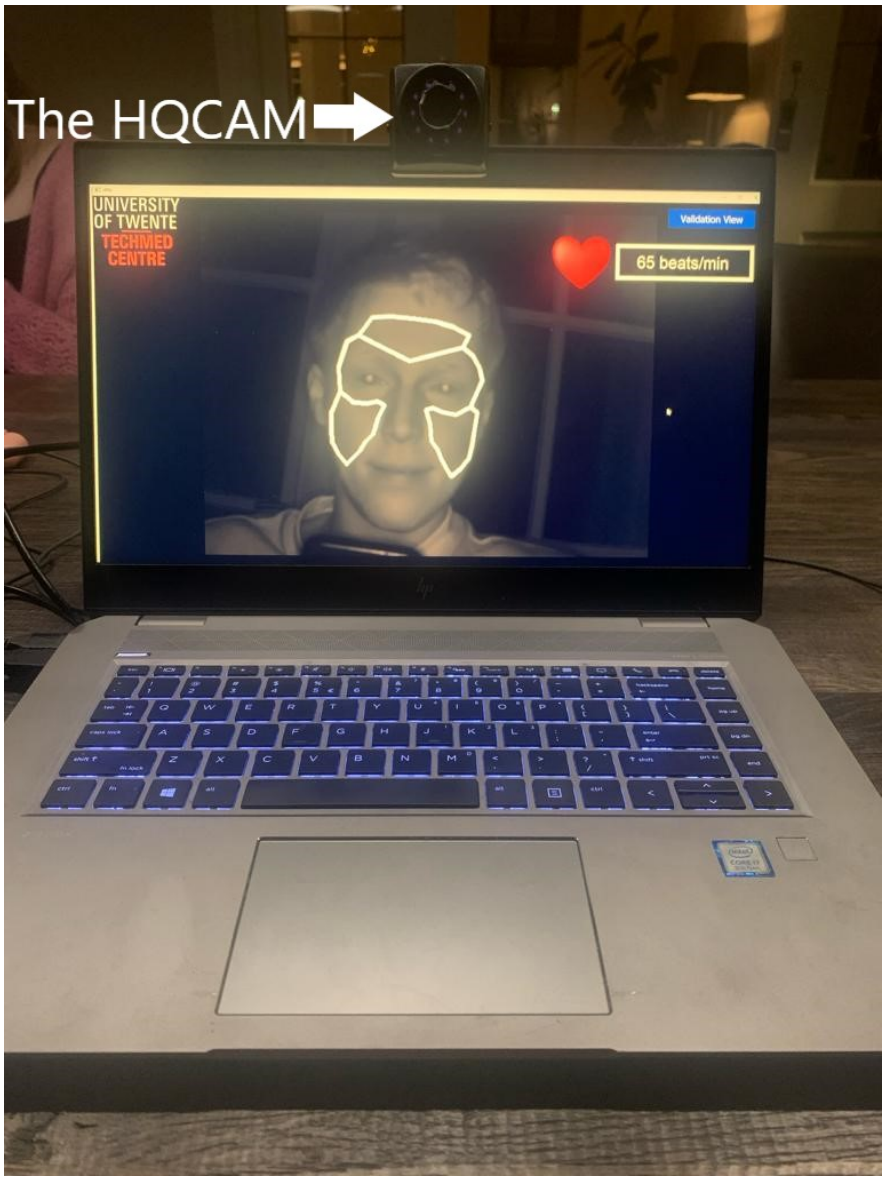

Figure 34: The demonstrator with the HQCAM placed on a laptop.

5 Discussion

5.1 rPPG Application Optimization

5.1.1 Camera

During the optimization process it became apparant that the impact of the camera on the accuracy of our rPPG application is significant. A notable difference was observed between the Sony a6000 (1920 x 1080 pixels, 60 fps) and the HP webcam (640×480 pixels, 30 fps) in terms of the HRE and SNR when detecting heart rate under ambient conditions. The ANOVA test revealed a significant difference ($P < 0.001$) in the SNRa between the HP Webcam and the Sony a6000, suggesting that camera resolution plays a crucial role in performance. This finding is consistent with existing literature, which underscores the importance of hardware selection in rPPG systems [85].

However, distinguishing the precise factor responsible for the performance variation between the HQCAM (1920×1080 pixels, 30 fps, 850 nm central wavelength) and the Sony NEX-5T (1920×1080 pixels, 60 fps, 940 nm central wavelength), whether frame rate or central wavelength, is challenging. Prior research indicates that frame rates exceeding thirty frames per second may not substantially enhance rPPG system performance [15]. Therefore, the minor discrepancies observed between the measurements with the Sony NEX-5T and the HQCAM could likely be attributed to differences in central wavelength. Future investigations should delve deeper into determining the optimal central wavelength for NIR-rPPG across various skin types.

Nevertheless, the results of the one-way ANOVA analysis between the SNRa of the NEX-5T and the HQCAM ($P = 0.13$) suggest no significant difference between the two NIR cameras. Considering the HQCAM's cost-effectiveness and built-in NIR light source, we opted to proceed with this camera for further experimentation.

5.1.2 Noise, Motion Artefacts and the Environment

The angle of illumination plays a crucial role in both the HRE and the SNR. Our observations indicate that as the angle of illumination increases, the HRE tends to increase while the SNR decreases. The most accurate results were obtained when the illumination angle was zero degrees (head-on). Consequently, we opted to maintain this illumination angle for the continuation of our research.

The unexpected influence of NIR light intensity on the SNR, as observed in our experiments, challenges our initial assumptions. Contrary to our expectations, increasing the NIR intensity with the NIR flashlight led to a decrease in the SNR. This unexpected effect could potentially be attributed to the introduction of undesirable noise by the flashlight source. Therefore, further investigation into the relationship between NIR light intensity and its impact on the

SNR is warranted.

On a positive note, tests conducted solely with the NIR-LEDs yielded promising results for both the HRE and SNR, as compared to our predefined interpretations outlined in Tables 2 and 3. This suggests that our rPPG application can effectively operate independently of ambient light conditions. This assertion is supported by the results of the one-way ANOVA, which revealed no significant difference in SNRa values between NIR-LEDs in a dark room and NIR-LEDs with ambient light (P = .42). Despite these findings, we opted to proceed with subsequent experiments using NIR-LEDs in conjunction with the NIR light present in the ambient light due to practical considerations.

Testing the different levels of gain proved difficult while also trying to maintain the delicate balance between achieving optimal brightness levels (between 100 and 150 [66]) and, at the same time, preserving the signal integrity. Contrary to our expectations, we were unable to discern a clear relationship in our data where increasing the gain level would correspondingly increase noise levels. This difficulty in manipulating the gain level without compromising the signal quality highlights the intricate nature of parameter fine-tuning in rPPG systems.

Our findings reinforce the advantages of fixing the ROI by stabilizing the head during rPPG signal acquisition, resulting in reduced HRE and improved SNR. This underscores the importance of minimizing head movement to enhance signal stability and quality. Practically, these observations suggest that the ROI tracking function of our application could be enhanced and warrants improvement.

5.1.3 Stability

Employing the Chebyshev Type 2 filter with an order of 4 has proven to yield the most favorable HRE and SNR among the tested bandpass filters, as indicated by the findings of Guler et al. [69]. This underscores the importance of signal processing techniques in refining rPPG signals. The impact of the frequency range of this bandpass filter aligns with our expectations; the narrowest frequency range of 45-120 exhibited the lowest HRE and highest SNR. However, adopting this frequency range would limit heart rate measurements to below 120 beats per minute. Additionally, with a p-value of P = .10 for the one-way ANOVA of the SNRa values between the frequency ranges of 45-120 and 45-180, no significant difference is observed. Consequently, we opted for the frequency range of 45-180, as it could yield similar results in HRE and SNR while accommodating heart rates exceeding 120 beats per minute.

Concerning the window size of the moving average filter, the ten-second window demonstrated superior performance in terms of both HRE and SNR. Smaller window sizes likely encountered heightened susceptibility to noise and erratic variations due to their higher temporal resolution. Conversely, larger window sizes might compromise the ability to capture rapid physiological changes. The ten-second window strikes a balance by facilitating the identification of both short-term variations and long-term trends in the rPPG signal.

The POS algorithm emerged as the most effective rPPG algorithm, exhibiting the lowest

HRE and the highest SNR under both ambient and NIR conditions. This aligns with findings from Wang et al., where the POS algorithm outperformed several other algorithms [60]. The effectiveness of the POS algorithm lies in its capability to eliminate specular components, resulting in reduced noise levels. Notably, the performance of the POS method did not significantly deteriorate under NIR conditions compared to ambient conditions, as indicated by a p-value of P = .05 from the one-way ANOVA. The CHROM algorithm was excluded from the results as it failed to measure the heart rate within the specified thirty-second time frame for the measurements. Future investigations may explore the CHROM method using a PC with greater computational capabilities. The GREEN and NIR algorithm exhibited poor performance under NIR conditions. This poor performance can be dedicated to the fact that both these algorithms only make use of one color channel and make no attempt to eliminate the specular component of the light.

5.2 Tests with Human Subjects with varying Skin Types

5.2.1 Influence of Skin Type

During the testing with the eighteen test subjects an improvement was observed in HRE and SNR for individuals with skin type VI when transitioning from ambient light conditions to NIR-rPPG; this improvement is significant, with $P < 0.001$.

In contrast to the positive outcomes observed for skin type VI, our results reveal an increase in HRE and a decrease in SNR for the other skin type categories when transitioning from ambient to NIR conditions. However, it is noteworthy that the measurements still fall within the acceptable range interpreted from the literature despite these changes. This suggests that our rPPG method is robust enough to deliver reliable heart rate estimations across different skin types.

With the p-values of the one-way ANOVA of the SNR values of the rPPG measurements under NIR (940 nm) conditions between the different skin type categories all exceeding 0.05, we can infer that our rPPG method is skin type invariant. There is no significant difference in function observed across the various skin type categories. However, this is not the case for the ambient measurements, as the p-value for skin type VI compared to the other categories is $P < 0.001$.

5.2.2 The Reference Measurement

Comparing the 95% confidence interval of the HRE for all test subjects, ranging from -6.1% to 6.2%, with the accuracy of ± two beats per minute of the finger pulse oximeter, suggests that our rPPG application approaches similar accuracy levels. It's important to note that while the finger pulse oximeter is commonly used as a reference measurement, the gold standard for measuring heart rate is ECG. Despite that our research employs two methods reliant on photoplethysmography, we decided for practical reasons, to continue using the finger pulse oximeter as the reference measurement in this study.

5.2.3 Future Research

The potential influence of breathing on rPPG signals presents a crucial consideration. The observed decrease in SNR after having the test subjects walk up and down the stairs suggests a potential impact of respiration on the measurements. Recognizing the significance of respiration rate and exploring higher cut-off frequencies could be essential in mitigating respiratory artefacts. Future research endeavors should focus on developing methods to integrate respiration rate data into rPPG algorithms, thereby enhancing the robustness and accuracy of the measurements.

The initial plan to test the rPPG application's performance in higher heart rate zones was not executed as intended. This was due to the test subjects' heart rates returning to their resting levels too quickly after walking up and down the stairs. For future research endeavors, the measurement protocol could be adapted to include exercise-induced scenarios using equipment like a home trainer or similar methods. This approach would enable the assessment of rPPG technology's performance in dynamic physiological conditions, enhancing its applicability in real-world scenarios where heart rates are elevated.

While our research has demonstrated the robustness of the rPPG application in terms of its independence from skin tone and environmental light conditions, it is important to note that further testing is required before its suitability for clinical practice can be confirmed. Notably, the application has not yet been evaluated in higher heart rate zones and under conditions of extreme heart rate variations. Furthermore, movement, a common occurrence in clinical settings, has been limited in our tests. Evaluating the performance of the rPPG application under conditions of movement is essential to ascertain its practical viability in real-world scenarios. The decrease in accuracy of the heart rate estimation when motion occurred during the measurements, indicates that additional research is needed into motion artefact suppression. Additionally, the size of our subject pool remains relatively small, warranting further investigation with a larger and more diverse sample population. These factors highlight the need for continued research and validation efforts to ensure the reliability and efficacy of the rPPG technology in clinical settings.

5.3 Application and Demonstrator Design

The graphical user interface (GUI) of the rPPG application was designed to emulate the experience of looking into a mirror while simultaneously having your heart rate measured. In the center of the screen, real-time video is displayed, providing users with a familiar visual feedback. Adjacent to the video feed, the measured heart rate is displayed in a white box, accompanied by a GIF of a beating heart to enhance user engagement. The application's background is kept black to ensure that the user's focus remains on the camera image and the displayed heart rate. To further enhance the GUI and provide more options, transitioning from PyQt5 to the newly released PyQt6 would be advisable. PyQt is a Python binding of a GUI toolkit, and upgrading to PyQt6 will offer additional features and improvements.

In the camera properties window, users have the flexibility to adjust various camera settings

to ensure optimal performance. Specifically, users can fine-tune properties such as brightness, aiming to maintain levels within the recommended range of 100 to 150 as advised by Odinaev et al. [66]. The impact of these adjustments can be visualized in real-time within the validation view window, where users can monitor the signal quality through the SQI value and the FFT spectrum. The validation window is meant to give more experienced users more insights into the quality of the signal. Additionally, users have the option to generate a spectrogram by clicking the corresponding button, providing a comprehensive visualization of the captured signal up to that point. Spectrograms can reveal periodic patterns in the signal corresponding to the heart rate and can be used to assess the quality of the signal. Anomalies or irregularities in the spectrogram may indicate poor signal quality. To improve the application, we would like to find a Python module to create a real-time spectrogram.

To enhance the user experience and create a more immersive setup, for when it is used during an exhibition like the Open Days at the University of Twente, we propose mounting the HQCAM on a larger display screen instead of solely on a laptop. By connecting the display screen to a PC running the rPPG application, users can enjoy a mirror-like experience while simultaneously monitoring their heart rate. This larger demonstrator not only provides a more engaging interaction but also offers greater visibility and ease of use for users during heart rate measurements.

6 Conclusion

In this master thesis, we delved into the realm of remote photoplethysmography (rPPG), with a particular focus on near-infrared remote photoplethysmography. Our aim was to comprehensively understand its performance, adaptability, and potential applications. The central objective was to determine whether near-infrared rPPG could serve as a reliable method for non-contact heart rate measurement, regardless of variations in skin tone and ambient light conditions. Through meticulous optimization processes and experiments involving human test subjects, our investigation has yielded valuable insights into the capabilities and challenges associated with this technology.

During the optimization phase, we identified the optimal parameters and settings essential for our research scope. The HQCAM emerged as the chosen camera for our experiments with human subjects. Additionally, after evaluating various rPPG algorithms, the POS algorithm stood out as the most promising candidate. Among the digital signal filters tested, the Chebyshev Type 2 filter with order 4 demonstrated the best performance in terms of HRE and SNR.

Our rPPG application has showcased independence from environmental light in NIR conditions. We observed no significant difference between measurements conducted in the dark, illuminated solely by NIR LEDs, and those conducted under ambient light conditions.

Furthermore, our rPPG application has demonstrated robustness across various skin tones in NIR conditions. While ambient rPPG showed significant disparities in HRE and SNR values for different skin types on the Fitzpatrick scale, NIR rPPG exhibited consistent performance across all skin types. Notably, while HRE and SNR values for skin type categories I - II and III - IV - V saw minor deteriorations, significant improvements were observed for skin type VI.

We developed a demonstrator where the HQCAM is positioned atop a laptop, connected via USB cable, allowing the rPPG application to run seamlessly. The application functions akin to a mirror, with the user's measured heart rate displayed alongside their "reflection."

For future research endeavors, exploring the functionality of the rPPG application in higher heart rate zones, such as through exercise sessions on a home trainer, could provide valuable insights. Additionally, determining the optimal NIR wavelength for NIR-rPPG could enhance the technology's accuracy and applicability. Ultimately, enhancing the study's validity and generalizability could be achieved by expanding the sample size and diversifying the participant demographics.

7 References

[1] Kai Zhang and Wenjie Ling. "Health Monitoring of Human Multiple Physiological Parameters Based on Wireless Remote Medical System". In: *IEEE Access* 8 (2020), pp. 71146–71159. DOI: 10.1109/ACCESS.2020.2987058.

[2] Gerald D Buckberg et al. "What Is the Heart? Anatomy, Function, Pathophysiology, and Misconceptions." eng. In: *Journal of cardiovascular development and disease* 5.2 (2018). ISSN: 2308-3425 (Electronic). DOI: 10.3390/jcdd5020033.

[3] Saif Ahmad et al. "Clinical review: A review and analysis of heart rate variability and the diagnosis and prognosis of infection". In: *Critical Care* 13.6 (2009), p. 232. ISSN: 1364-8535. DOI: 10.1186/cc8132. URL: https://doi.org/10.1186/cc8132.

[4] P K Biswas et al. "Heart rate variability in dilated cardiomyopathy." eng. In: *Indian heart journal* 52.2 (2000), pp. 187–191. ISSN: 0019-4832 (Print).

[5] May Thu Kyaw and Zay Maung Maung. *Hypokalemia-Induced Arrhythmia: A Case Series and Literature Review.* eng. 2022. DOI: 10.7759/cureus.22940.

[6] Brittney A Grella et al. *Lyme Carditis: A Rare Presentation of Sinus Bradycardia Without Any Conduction Defects.* eng. 2019. DOI: 10.7759/cureus.5554.

[7] Walter A Parham et al. "Hyperkalemia revisited." eng. In: *Texas Heart Institute journal* 33.1 (2006), pp. 40–47. ISSN: 0730-2347 (Print).

[8] George E Billman. "Heart rate variability - a historical perspective." eng. In: *Frontiers in physiology* 2 (2011), p. 86. ISSN: 1664-042X (Electronic). DOI: 10.3389/fphys.2011.00086.

[9] Rachel Hajar. "The Pulse from Ancient to Modern Medicine: Part 3." eng. In: *Heart views : the official journal of the Gulf Heart Association* 19.3 (2018), pp. 117–120. ISSN: 1995-705X (Print). DOI: 10.4103/HEARTVIEWS.HEARTVIEWS_16_19.

[10] Christian Cajavilca and Joseph Varon. "Willem Einthoven: The development of the human electrocardiogram". In: *Resuscitation* 76.3 (2008), pp. 325–328. ISSN: 0300-9572. DOI: https://doi.org/10.1016/j.resuscitation.2007.10.014. URL: https://www.sciencedirect.com/science/article/pii/S0300957207005813.

[11] Majd AlGhatrif and Joseph Lindsay. "A brief review: history to understand fundamentals of electrocardiography". In: *Journal of Community Hospital Internal Medicine Perspectives* 2.1 (2012), p. 14383. ISSN: null. DOI: 10.3402/jchimp.v2i1.14383. URL: https://doi.org/10.3402/jchimp.v2i1.14383.

[12] Rony Vincent. "From a laboratory to the wearables: a review on history and evolution of electrocardiogram". In: *Iberoamerican Journal of Medicine* 4 (Sept. 2022), pp. 248–255. DOI: 10.53986/ibjm.2022.0038.

[13] Aymen A Alian and Kirk H Shelley. "Photoplethysmography". In: *Best Practice Research Clinical Anaesthesiology* 28.4 (2014), pp. 395–406. ISSN: 1521-6896. DOI: https://doi.org/10.1016/j.bpa.2014.08.006. URL: https://www.sciencedirect.com/science/article/pii/S1521689614000755.

[14] A Jubran. "Pulse oximetry." eng. In: *Critical care (London, England)* 3.2 (1999), R11–R17. ISSN: 1466-609X (Electronic). DOI: 10.1186/cc341.

[15] Akito Tohma et al. "Evaluation of Remote Photoplethysmography Measurement Conditions toward Telemedicine Applications". In: *Sensors* 21.24 (2021). ISSN: 1424-8220. DOI: 10.3390/s21248357. URL: https://www.mdpi.com/1424-8220/21/24/8357.

[16] T. Sivani and Sushruta Mishra. "Wearable Devices: Evolution and Usage in Remote Patient Monitoring System". In: May 2022, pp. 311–332. ISBN: 978-3-030-97928-7. DOI: 10.1007/978-3-030-97929-4_14.

[17] Korosh Vatanparvar et al. "Respiration Rate Estimation from Remote PPG via Camera in Presence of Non-Voluntary Artifacts". In: *2022 IEEE-EMBS International Conference on Wearable and Implantable Body Sensor Networks (BSN)*. 2022, pp. 1–4. DOI: 10.1109/BSN56160.2022.9928485.

[18] Gerardo H Martinez-Delgado et al. "Measuring Heart Rate Variability Using Facial Video". In: *Sensors* 22.13 (2022). ISSN: 1424-8220. DOI: 10.3390/s22134690. URL: https://www.mdpi.com/1424-8220/22/13/4690.

[19] E M Nowara, D McDuff, and A Veeraraghavan. "A Meta-Analysis of the Impact of Skin Type and Gender on Non-contact Photoplethysmography Measurements". In: *2020 IEEE/CVF Conference on Computer Vision and Pattern Recognition Workshops (CVPRW)*. 2020, pp. 1148–1155. ISBN: 2160-7516 VO -. DOI: 10.1109/CVPRW50498.2020.00150.

[20] Wenjin Wang and Albertus C den Brinker. "Modified RGB Cameras for Infrared Remote-PPG". In: *IEEE Transactions on Biomedical Engineering* 67.10 (2020), pp. 2893–2904. DOI: 10.1109/TBME.2020.2973313.

[21] David Martínez. *Spectroelectrochemistry*. 2021. URL: https://www.metrohm.com/en_nl/discover/blog/20-21/spectroelectrochemistry--shedding-light-on-the-unknown.html.

[22] Navin Kumar et al. "Continuous vital sign analysis for predicting and preventing neonatal diseases in the twenty-first century: big data to the forefront." eng. In: *Pediatric research* 87.2 (2020), pp. 210–220. ISSN: 1530-0447 (Electronic). DOI: 10.1038/s41390-019-0527-0.

[23] Jeffrey M Perlman et al. "Part 11: Neonatal resuscitation: 2010 International Consensus on Cardiopulmonary Resuscitation and Emergency Cardiovascular Care Science With Treatment Recommendations." eng. In: *Circulation* 122.16 Suppl 2 (2010), S516–38. ISSN: 1524-4539 (Electronic). DOI: 10.1161/CIRCULATIONAHA.110.971127.

[24] Emily Phillipos et al. "Heart Rate Assessment Immediately after Birth." eng. In: *Neonatology* 109.2 (2016), pp. 130–138. ISSN: 1661-7819 (Electronic). DOI: 10.1159/000441940.

[25] U Blume-Peytavi et al. “Fragility of epidermis in newborns, children and adolescents.” eng. In: *Journal of the European Academy of Dermatology and Venereology : JEADV* 30 Suppl 4 (2016), pp. 3–56. ISSN: 1468-3083 (Electronic). DOI: 10.1111/jdv.13636.

[26] Margaret Broom, Ann Marie Dunk, and Abdel-Latif E Mohamed. “Predicting Neonatal Skin Injury: The First Step to Reducing Skin Injuries in Neonates.” eng. In: *Health services insights* 12 (2019), p. 1178632919845630. ISSN: 1178-6329 (Print). DOI: 10.1177/1178632919845630.

[27] Neotech. *Mini NeoLead*. URL: https://www.neotechproducts.com/product/mini-neolead/.

[28] Anouk W. J. Scholten et al. “Feasibility of wireless cardiorespiratory monitoring with dry electrodes incorporated in a belt in preterm infants”. English. In: *Physiological measurement* 43.5 (May 2022). Publisher Copyright: © 2022 Institute of Physics and Engineering in Medicine. ISSN: 0967-3334. DOI: https://doi.org/10.1088/1361-6579/ac69a9.

[29] Carmen M Lorente Flores et al. “The Effects of a New Wireless Non-Adhesive Cardiorespiratory Monitoring Device on the Skin Conditions of Preterm Infants”. In: *Sensors* 24.4 (2024). ISSN: 1424-8220. DOI: 10.3390/s24041258. URL: https://www.mdpi.com/1424-8220/24/4/1258.

[30] Anna Matas et al. “Melanin as a confounding factor in near infrared spectroscopy of skin”. In: *Vibrational Spectroscopy* 28.1 (2002), pp. 45–52. ISSN: 0924-2031. DOI: https://doi.org/10.1016/S0924-2031(01)00144-8. URL: https://www.sciencedirect.com/science/article/pii/S0924203101001448.

[31] Jordan P Farkas, John E Hoopman, and Jeffrey M Kenkel. “Five Parameters You Must Understand to Master Control of Your Laser/Light-Based Devices”. In: *Aesthetic Surgery Journal* 33.7 (2013), pp. 1059–1064. ISSN: 1090-820X. DOI: 10.1177/1090820X13501174. URL: https://doi.org/10.1177/1090820X13501174.

[32] GembaRed. *How deep do red and near-infrared wavelengths penetrate into the body.* 2021. URL: https://gembared.com/blogs/musings/how-deep-does-red-and-near-infrared-wavelengths-penetrate-into-the-body-marketing-vs-science.

[33] Piyu Parth Naik and Syed Nadir Farrukh. “Influence of Ethnicities and Skin Color Variations in Different Populations: A Review.” eng. In: *Skin pharmacology and physiology* 35.2 (2022), pp. 65–76. ISSN: 1660-5535 (Electronic). DOI: 10.1159/000518826.

[34] Mette Henriksen Ravnbak. “Objective determination of Fitzpatrick skin type”. In: *Dan Med Bull* 57.8 (2010), B4153.

[35] ENRICHCLINIC. *What is Fitzpatrick skin type?* URL: https://www.enrichclinic.com.au/what-is-fitzpatrick-skin-type/.

[36] Valery Tuchin. “Tissue Optics Light Scattering Methods and Instruments for Medial Diagnosis”. In: *SPIE* 13 (2000). DOI: 10.1117/3.684093.

[37] Valery Tuchin. “Tissue Optics and Photonics: Light-Tissue Interaction”. In: *Journal of Biomedical Photonics Engineering* 1 (2015), pp. 98–134. DOI: 10.18287/JBPE-2015-1-2-98.

[38] Igor Victorovich Meglinski and Stephen John Matcher. "Determination of absorption coefficient of skin melanin in visible and NIR spectral region". In: *Proc.SPIE*. Vol. 3907. 2000, pp. 143–150. DOI: 10.1117/12.386246. URL: https://doi.org/10.1117/12.386246.

[39] Louise Finlayson et al. "Depth Penetration of Light into Skin as a Function of Wavelength from 200 to 1000 nm." eng. In: *Photochemistry and photobiology* 98.4 (2022), pp. 974–981. ISSN: 1751-1097 (Electronic). DOI: 10.1111/php.13550.

[40] Jana Kainerstorfer et al. "Principal component model of multispectral data for near real-time skin chromophore mapping". In: *Journal of biomedical optics* 15 (2010), p. 46007. DOI: 10.1117/1.3463010.

[41] Meir Nitzan, Itamar Nitzan, and Yoel Arieli. "The Various Oximetric Techniques Used for the Evaluation of Blood Oxygenation." eng. In: *Sensors (Basel, Switzerland)* 20.17 (2020). ISSN: 1424-8220 (Electronic). DOI: 10.3390/s20174844.

[42] Chun-Hong Cheng et al. "Deep Learning Methods for Remote Heart Rate Measurement: A Review and Future Research Agenda". In: *Sensors* 21 (2021), p. 6296. DOI: 10.3390/s21186296.

[43] Shoji Tominaga. "Dichromatic reflection models for a variety of materials". In: *Color Research Application* 19.4 (1994), pp. 277–285. ISSN: 0361-2317. DOI: https://doi.org/10.1002/col.5080190408. URL: https://doi.org/10.1002/col.5080190408.

[44] John Allen. "Photoplethysmography and its application in clinical physiological measurement." eng. In: *Physiological measurement* 28.3 (2007), R1–39. ISSN: 0967-3334 (Print). DOI: 10.1088/0967-3334/28/3/R01.

[45] G de Haan and V Jeanne. "Robust Pulse Rate From Chrominance-Based rPPG". In: *IEEE Transactions on Biomedical Engineering* 60.10 (2013), pp. 2878–2886. ISSN: 1558-2531 VO - 60. DOI: 10.1109/TBME.2013.2266196.

[46] John Allen and Alan Murray. "Variability of photoplethysmography peripheral pulse measurements at the ears, thumbs and toes". In: *Science, Measurement and Technology, IEE Proceedings* - 147 (2000), pp. 403–407. DOI: 10.1049/ip-smt:20000846.

[47] R Yunifar et al. "Preliminary Studies Comparing Heart Rate Measurement Using Optical Sensor Based on Self Mixing Interferometry and Photoplethysmography (PPG)". In: *Journal of Physics: Conference Series* 1505 (Mar. 2020), p. 012072. DOI: 10.1088/1742-6596/1505/1/012072.

[48] Sebastian Zaunseder et al. "Cardiovascular assessment by imaging photoplethysmography - a review." eng. In: *Biomedizinische Technik. Biomedical engineering* 63.5 (2018), pp. 617–634. ISSN: 1862-278X (Electronic). DOI: 10.1515/bmt-2017-0119.

[49] Benjamin Kossack et al. "Perfusion assessment via local remote photoplethysmography (rPPG)". In: *2022 IEEE/CVF Conference on Computer Vision and Pattern Recognition Workshops (CVPRW)* (2022), pp. 2191–2200.

[50] Sander Soo. "Object detection using Haar-cascade Classifier". In: *Institute of Computer Science, University of Tartu* 2.3 (2014), pp. 1–12.

[51] P Viola and M Jones. "Rapid object detection using a boosted cascade of simple features". In: *Proceedings of the 2001 IEEE Computer Society Conference on Computer Vision and Pattern Recognition. CVPR 2001*. Vol. 1. 2001, pp. I–I. DOI: 10.1109/CVPR.2001.990517.

[52] B Thaman, T Cao, and N Caporusso. "Face Mask Detection using MediaPipe Facemesh". In: *2022 45th Jubilee International Convention on Information, Communication and Electronic Technology (MIPRO)*. 2022, pp. 378–382. DOI: 10.23919/MIPRO55190.2022.9803531.

[53] Li Cuimei et al. "Human face detection algorithm via Haar cascade classifier combined with three additional classifiers". In: *2017 13th IEEE International Conference on Electronic Measurement Instruments (ICEMI)*. 2017, pp. 483–487. DOI: 10.1109/ICEMI.2017.8265863.

[54] Shivalila Hangaragi, Tripty Singh, and Neelima N. "Face Detection and Recognition Using Face Mesh and Deep Neural Network". In: *Procedia Computer Science* 218 (2023), pp. 741–749. ISSN: 1877-0509. DOI: https://doi.org/10.1016/j.procs.2023.01.054. URL: https://www.sciencedirect.com/science/article/pii/S1877050923000546.

[55] Yan Chen et al. *Use Moving Average Filter to Reduce Noises in Wearable PPG During Continuous Monitoring*. Vol. 181. 2016, pp. 193–203. ISBN: 978-3-319-49654-2. DOI: 10.1007/978-3-319-49655-9_26.

[56] Dae-Yeol Kim, Kwangkee Lee, and Chae-Bong Sohn. "Assessment of ROI Selection for Facial Video-Based rPPG." eng. In: *Sensors (Basel, Switzerland)* 21.23 (2021). ISSN: 1424-8220 (Electronic). DOI: 10.3390/s21237923.

[57] Sam Proell. *yarppg*. 2019. URL: https://github.com/SamProell/yarppg.

[58] L Tarassenko et al. "Non-contact video-based vital sign monitoring using ambient light and auto-regressive models." eng. In: *Physiological measurement* 35.5 (2014), pp. 807–831. ISSN: 1361-6579 (Electronic). DOI: 10.1088/0967-3334/35/5/807.

[59] G Boccignone et al. "An Open Framework for Remote-PPG Methods and Their Assessment". In: *IEEE Access* 8 (2020), pp. 216083–216103. ISSN: 2169-3536 VO - 8. DOI: 10.1109/ACCESS.2020.3040936.

[60] W Wang et al. "Algorithmic Principles of Remote PPG". In: *IEEE Transactions on Biomedical Engineering* 64.7 (2017), pp. 1479–1491. ISSN: 1558-2531 VO - 64. DOI: 10.1109/TBME.2016.2609282.

[61] Yunda Zheng et al. "Optimal PSF Estimation for Simple Optical System Using a Wide-Band Sensor Based on PSF Measurement". In: *Sensors* 18.10 (2018). ISSN: 1424-8220. DOI: 10.3390/s18103552. URL: https://www.mdpi.com/1424-8220/18/10/3552.

[62] Wim Verkruysse, Lars O Svaasand, and J Stuart Nelson. "Remote plethysmographic imaging using ambient light." eng. In: *Optics express* 16.26 (2008), pp. 21434–21445. ISSN: 1094-4087 (Electronic). DOI: 10.1364/oe.16.021434.

[63] S Ray. *Scientific Photography and Applied Imaging*. Taylor & Francis, 1999. ISBN: 9781136094385. URL: https://books.google.nl/books?id=h6zMCgAAQBAJ.

[64] Ukcheol Shin et al. “Camera Exposure Control for Robust Robot Vision with Noise-Aware Image Quality Assessment”. In: *2019 IEEE/RSJ International Conference on Intelligent Robots and Systems (IROS)*. 2019, pp. 1165–1172. DOI: 10.1109/IROS40897.2019.8968590.

[65] Youngjin Yoo et al. “A digital ISO expansion technique for digital cameras”. In: *Proc.SPIE*. Vol. 7537. 2010, 75370U. DOI: 10.1117/12.838774. URL: https://doi.org/10.1117/12.838774.

[66] Ismoil Odinaev et al. “Optimizing Camera Exposure Control Settings for Remote Vital Sign Measurements in Low-Light Environments”. In: *2023 IEEE/CVF Conference on Computer Vision and Pattern Recognition Workshops (CVPRW)*. 2023, pp. 6086–6093. DOI: 10.1109/CVPRW59228.2023.00648.

[67] Rik van Esch et al. “Remote ppg for heart rate monitoring: lighting conditions and camera shutter time”. In: *43rd Annual International Conference of the IEEE Engineering in Medicine and Biology Society* (2021).

[68] Giovanni Cennini et al. “Heart rate monitoring via remote photoplethysmography with motion artifacts reduction”. In: *Optics Express* 18.5 (2010), pp. 4867–4875. DOI: 10.1364/OE.18.004867. URL: https://opg.optica.org/oe/abstract.cfm?URI=oe-18-5-4867.

[69] Saygun Guler et al. “Optimal digital filter selection for remote photoplethysmography (rPPG) signal conditioning.” eng. In: *Biomedical physics engineering express* 9.2 (2023). ISSN: 2057-1976 (Electronic). DOI: 10.1088/2057-1976/acaf8a.

[70] University of Pennsylvania. *The Discrete Fourier Transform*. Tech. rep. University of Pennsylvania. URL: https://www.seas.upenn.edu/~ese1500/spring2023/labs/Lab04.pdf.

[71] I W Selesnick and C S Burrus. “Generalized digital Butterworth filter design”. In: *IEEE Transactions on Signal Processing* 46.6 (1998), pp. 1688–1694. ISSN: 1941-0476 VO - 46. DOI: 10.1109/78.678493.

[72] Bilal Asad et al. “Improving Legibility of Motor Current Spectrum for Broken Rotor Bars Fault Diagnostics”. In: *Electrical, Control and Communication Engineering* 15 (2019), pp. 1–8. DOI: 10.2478/ecce-2019-0001.

[73] Mahesh Chavan, Ra Agarwala, and Mahadev Uplane. “Comparative Study of Chebyshev I and Chebyshev II Filter used For Noise Reduction in ECG Signal”. In: (2008).

[74] SilverCrest. *User Manual SPO55*. Tech. rep. URL: https://www.gebruikershandleiding.com/Silvercrest-IAN-297929---SPO55/preview-handleiding-872862.html.

[75] Jörg Kaufmann and A G Schering. “Analysis of Variance ANOVA”. In: *Wiley StatsRef: Statistics Reference Online*. 2014. ISBN: 9781118445112. DOI: https://doi.org/10.1002/9781118445112.stat06938. URL: https://doi.org/10.1002/9781118445112.stat06938.

[76] *About OpenCV*. URL: https://opencv.org/about/.

[77] *MediaPipe face detector*. URL: https://developers.google.com/mediapipe/solutions/vision/face_detector.

[78] Valentin Bazarevsky et al. *BlazeFace: Sub-millisecond Neural Face Detection on Mobile GPUs*. 2019.

[79] Dimitrios Kolosov et al. "Contactless Camera-Based Heart Rate and Respiratory Rate Monitoring Using AI on Hardware". In: *Sensors* 23 (May 2023), p. 4550. DOI: 10.3390/s23094550.

[80] MediaPipe. *Face landmark detection guide for Python*. 2023. URL: https://developers.google.com/mediapipe/solutions/vision/face_landmarker/python.

[81] R Krishnan, B Natarajan, and S Warren. "Two-Stage Approach for Detection and Reduction of Motion Artifacts in Photoplethysmographic Data". In: *IEEE Transactions on Biomedical Engineering* 57.8 (2010), pp. 1867–1876. ISSN: 1558-2531 VO - 57. DOI: 10.1109/TBME.2009.2039568.

[82] Mohamed Elgendi. "Optimal Signal Quality Index for Photoplethysmogram Signals." eng. In: *Bioengineering (Basel, Switzerland)* 3.4 (2016). ISSN: 2306-5354 (Print). DOI: 10.3390/bioengineering3040021.

[83] Mark van Gastel, Sander Stuijk, and Gerard de Haan. "Motion Robust Remote-PPG in Infrared". In: *IEEE Transactions on Biomedical Engineering* 62.5 (2015), pp. 1425–1433. DOI: 10.1109/TBME.2015.2390261.

[84] Fridolin Haugg, Mohamed Elgendi, and Carlo Menon. "GRGB rPPG: An Efficient Low-Complexity Remote Photoplethysmography-Based Algorithm for Heart Rate Estimation". In: *Bioengineering* 10.2 (2023). ISSN: 2306-5354. DOI: 10.3390/bioengineering10020243. URL: https://www.mdpi.com/2306-5354/10/2/243.

[85] Rencheng Song et al. "New insights on super-high resolution for video-based heart rate estimation with a semi-blind source separation method". In: *Computers in Biology and Medicine* 116 (2020), p. 103535. ISSN: 0010-4825. DOI: https://doi.org/10.1016/j.compbiomed.2019.103535. URL: https://www.sciencedirect.com/science/article/pii/S0010482519303944.

8 Appendix

8.1 Results of the Optimization of the rPPG Application

8.1.1 Cameras

In Figure 35 the HRE and the SNR, that have been determined with the measurements, of the different cameras are presented in bar charts. The Sony a6000 under ambient conditions performs the best in both metrics. The HP Webcam performs the worst in both metrics. The HRE of the HQCAM is lower than that of the Sony NEX-5T, as to where the SNR of the Sony NEX-5T is higher. The p-value for the ANOVA between the SNRa of the HP Webcam and the Sony a6000 is $P < .001$. The p-value for the one-way ANOVA between the SNRa of the NEX-5T and the HQCAM is $P = .13$.

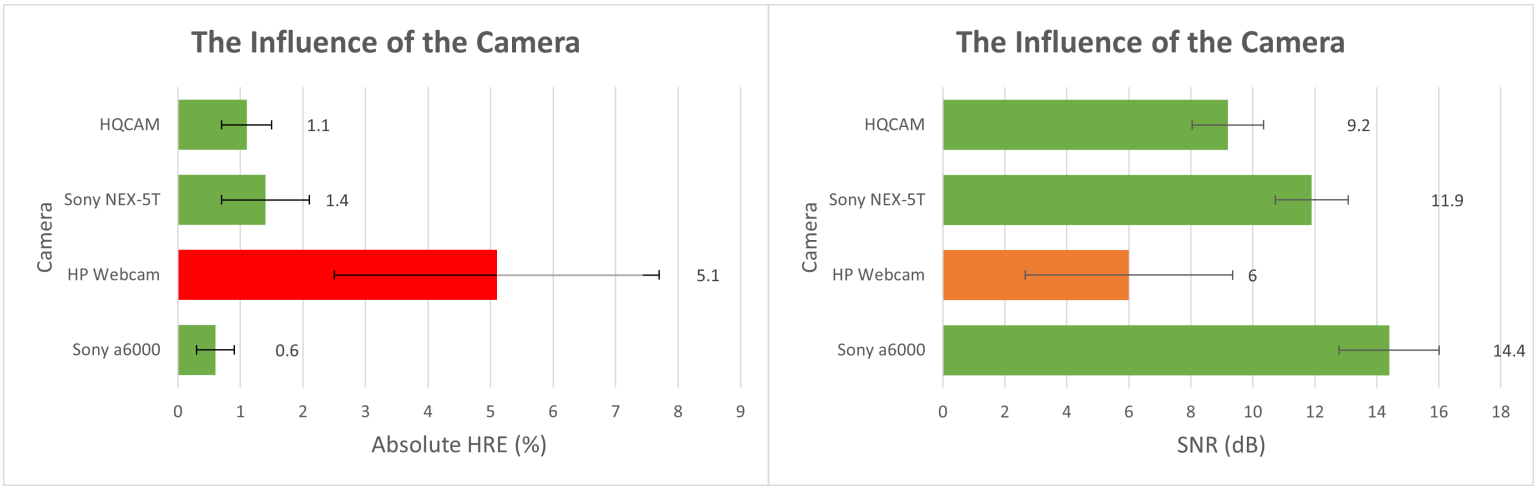

(a) The absolute HRE of the different cameras *(b) The SNR of the different cameras*

Figure 35: The evaluation metrics of the different cameras presented in bar charts, where the x-axis and y-axis denote the evaluation metrics and the different cameras, respectively.

8.1.2 Results Noise, Motion Artefacts and the Environment Tests

8.1.2.1 Angle of Illumination

A schematic representation of the angles of illumination is given in Figure 36. In Figure 37 HRE and SNR under different angles of illumination are presented. An angle of zero degrees indicates that the light source is perpendicular to the face of the test person. It shows that the heart rate is most accurately calculated when the angle of illumination is 0 degrees, this also delivers the highest SNR. An angle of illumination of 90 degrees gives the least accurate heart rate estimation with the lowest SNR. An increasing angle of illumination causes an increasing HRE and a decreasing SNR.

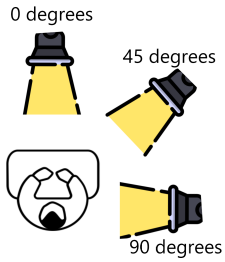

Figure 36: A schematic overview of illumination angles.

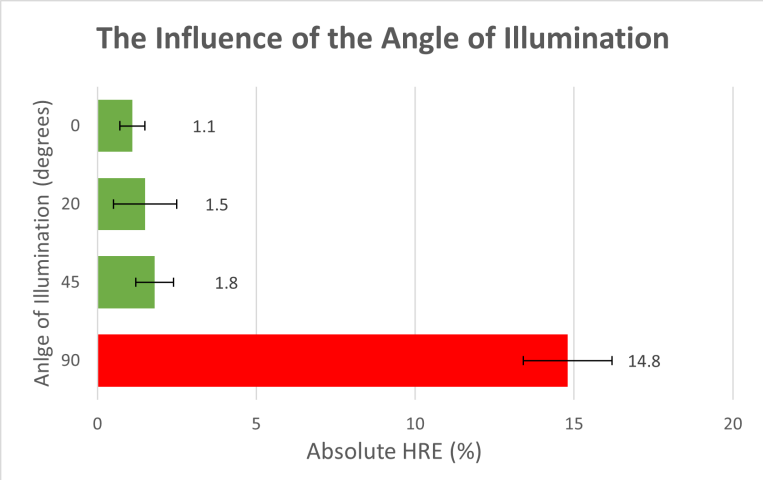

(a) The absolute HRE of the different illumination angles

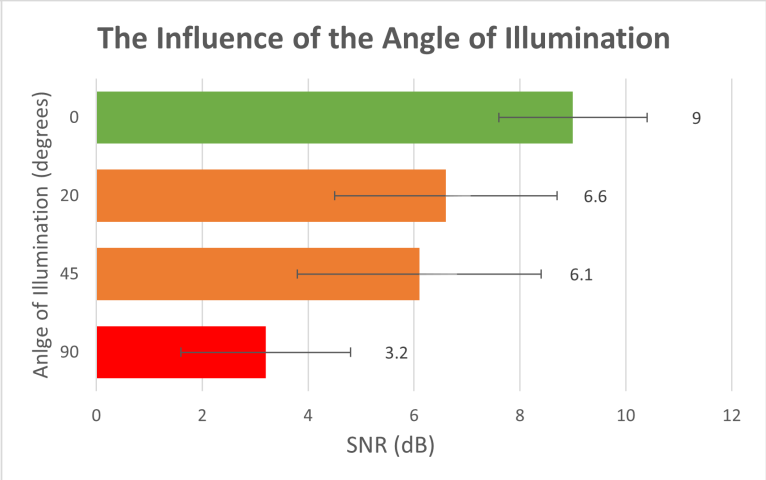

(b) The SNR of the different illumination angles

Figure 37: The evaluation metrics of the different angles of illumination, where the x-axis and y-axis denote the evaluation metrics and the different angles of illumination in degrees, respectively. The angle of zero degrees indicates that the light source is perpendicular to the face of the test person.

8.1.2.2 NIR Lighting

An overview of the results of the tests with the different NIR light sources is given in Figure 38. The combination of NIR illumination from environment light and the NIR-LEDs that

are integrated in the HQCAM give the highest SNR, where the use of only the NIR-LEDs in a dark room gives the lowest HRE. The additional use of a NIR flashlight causes an increase in the HRE and a decrease in the SNR. The p-value for the one-way ANOVA of the SNRa values between NIR-LEDs in a dark room and NIR-LEDs with environment light is P = .42.

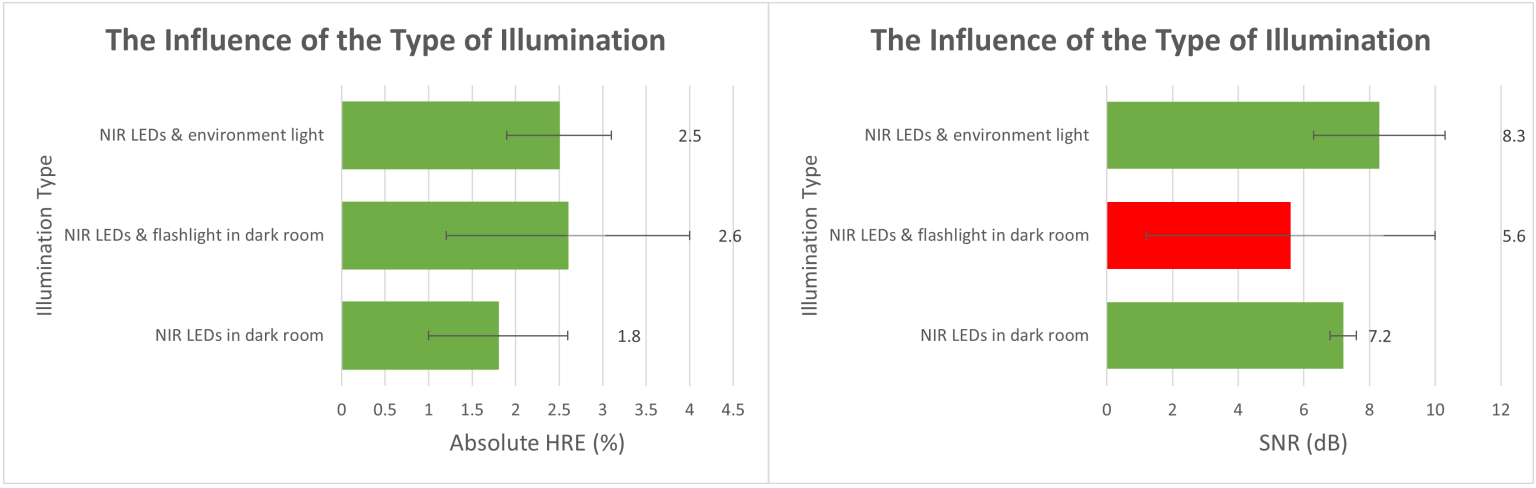

(a) The absolute HRE of the type of illumination *(b) The SNR of the type of illumination*

Figure 38: The evaluation metrics of the different types of illumination, where the x-axis and y-axis denote the evaluation metrics and the type of illumination, respectively.

8.1.2.3 Gain Level

The results of the measurements investigating the influence of the gain parameter are displayed in Figure 39. Gain levels five and eight show the lowest HRE, whereas gain level three shows the highest average SNR.

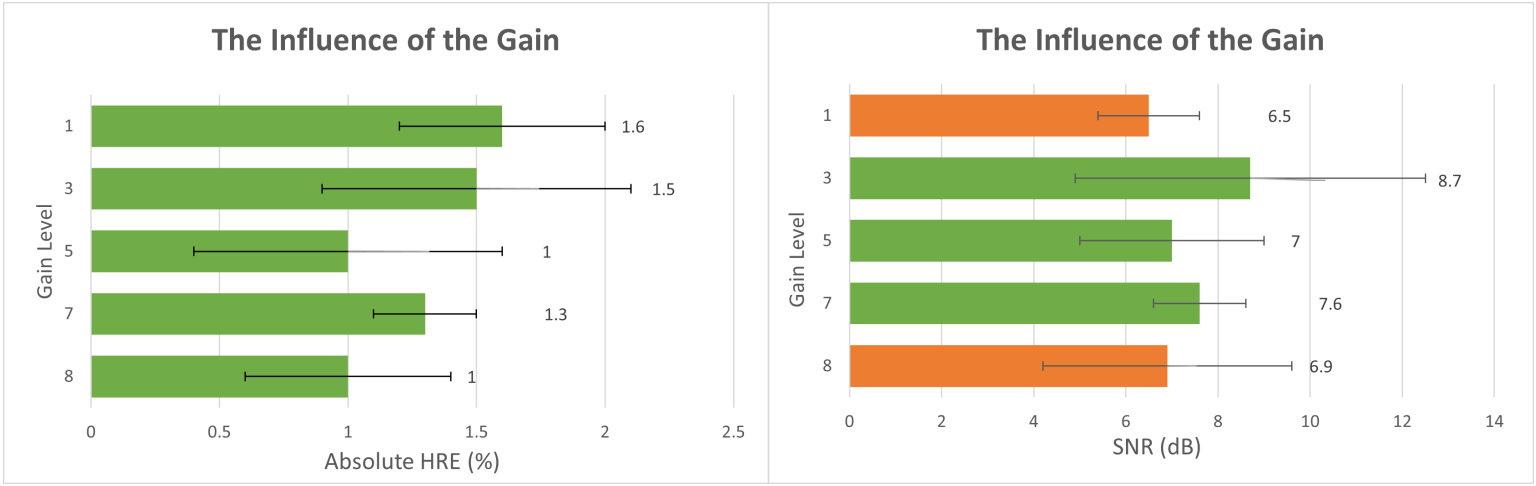

(a) The absolute HRE of the different gain levels *(b) The SNR of the different gain levels*

Figure 39: The evaluation metrics of the different gain levels, where the x-axis and y-axis denote the evaluation metrics and the different gain levels respectively.

8.1.2.4 Head Fixation

The influence of fixating the head on the HRE and SNR of rPPG measurements can be seen in Figure 40. A fixated head causes a lower HRE and a higher SNR compared with a loose head.

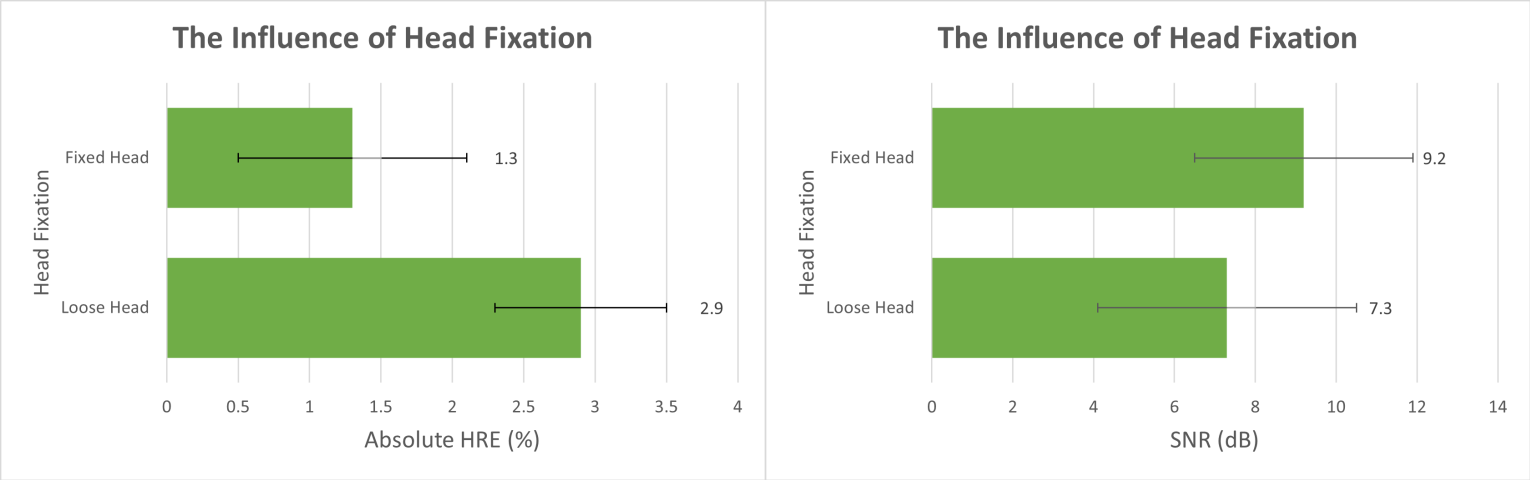

(a) The absolute HRE of the head fixation

(b) The SNR of the head fixation

Figure 40: The evaluation metrics of the head fixation, where the x-axis and y-axis denote the evaluation metrics and whether the head is fixated or loose, respectively.

8.1.3 Results Stability Tests

8.1.3.1 Bandpass Filters

The results of the measurements investigating the influence of the order of the Butterworth filters can be seen in Figure 41. The fourth order of the Butterworth filter gave the lowest HRE and the highest SNR, however the SNR value is relatively low.

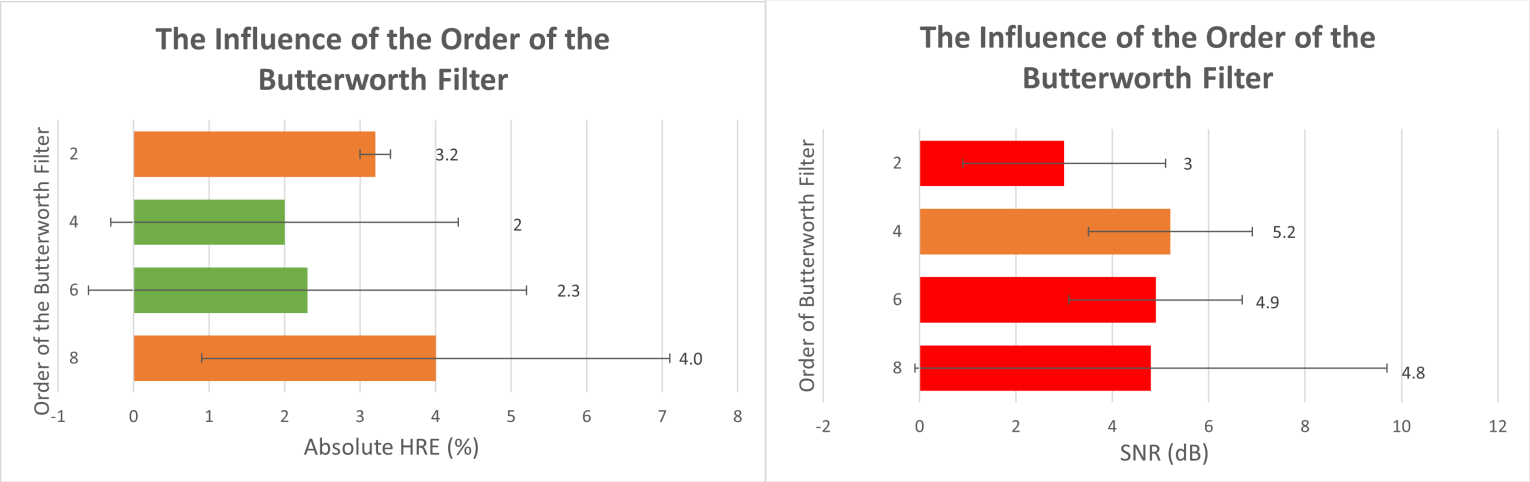

(a) The absolute HRE of the different Butterworth orders

(b) The SNR of the different Butterworth orders

Figure 41: The evaluation metrics of the different orders of the Butterworth filter, where the x-axis and y-axis denote the evaluation metrics and the order of the Butterworth filter, respectively.

Figure 42 shows the evaluation metrics of the different orders of the Chebyshev Type 2 filter. The fourth order of the Chebyshev Type 2 filter show the lowest HRE and the highest SNR value. Comparing these values with the ones of the best Butterworth order, it becomes clear that the fourth order of the Chebyshev Type 2 filter shows both the lowest HRE and the highest SNR.

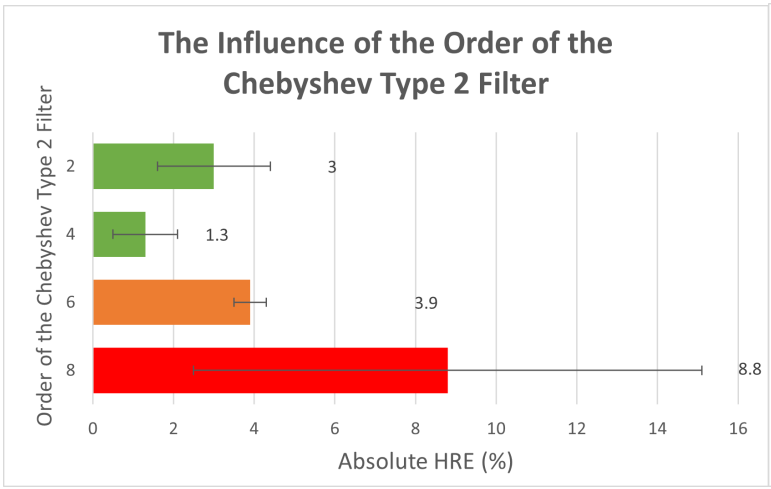

(a) The absolute HRE of the Chebyshev Type 2 orders

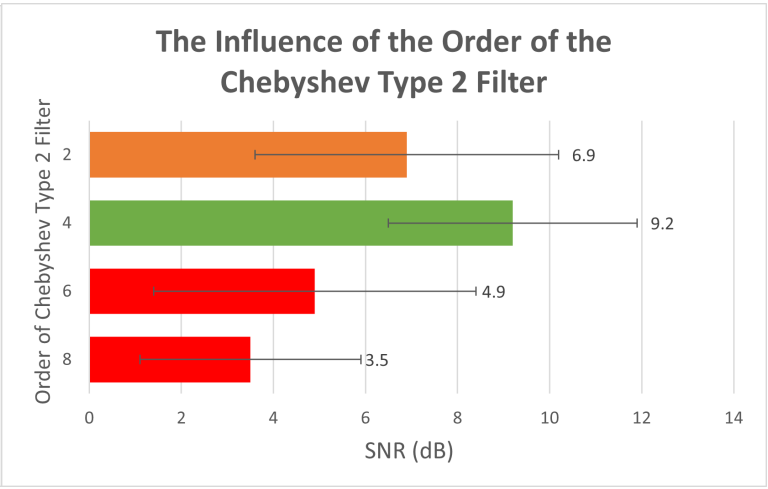

(b) The SNR of the Chebyshev Type 2 orders

Figure 42: The evaluation metrics of the different orders of the Chebyshev Type 2 filter, where the x-axis and y-axis denote the evaluation metrics and the order of the Chebyshev Type 2 filter, respectively.

8.1.3.2 Frequency Range

Figure 43 shows the evaluation metrics of the different frequency ranges that have been tested. The range from 45 to 120 Hertz gives both the lowest HRE and the highest SNR. The frequency range from 45 to 180 Hertz is the only other range tested that gives both a HRE and SNR value that can be considered good according to our interpretation in Table 2 and 3. The p-value for the one-way ANOVA of the SNRa values of the frequency range of 45-120 and 45-180 is P = .10.

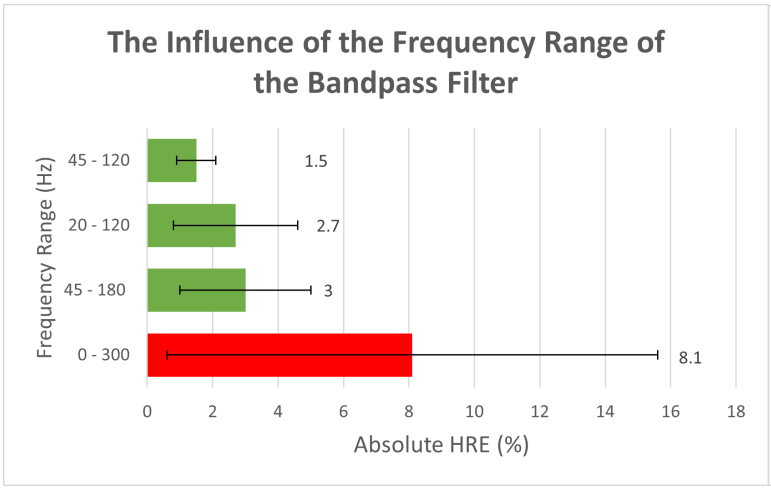

(a) The absolute HRE of the different frequency ranges

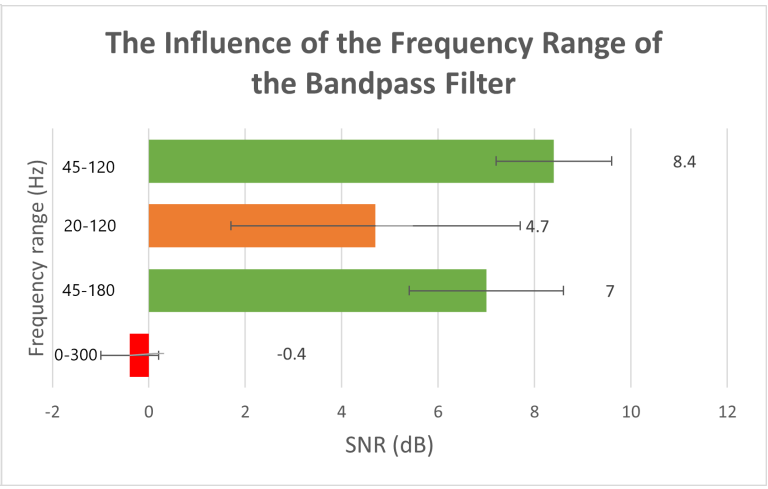

(b) The SNR of the different frequency ranges

Figure 43: The evaluation metrics of the different frequency ranges of the bandpass filter, where the x-axis and y-axis denote the evaluation metrics and the different frequency ranges in Hertz, respectively.

8.1.3.3 Window Size of the Moving Average Filter

The results of the measurements investigating the influence of the window size of the moving average filter on the HRE and SNR are displayed in Figure 44. The window size of 10 seconds shows both the lowest HRE and the highest SNR.

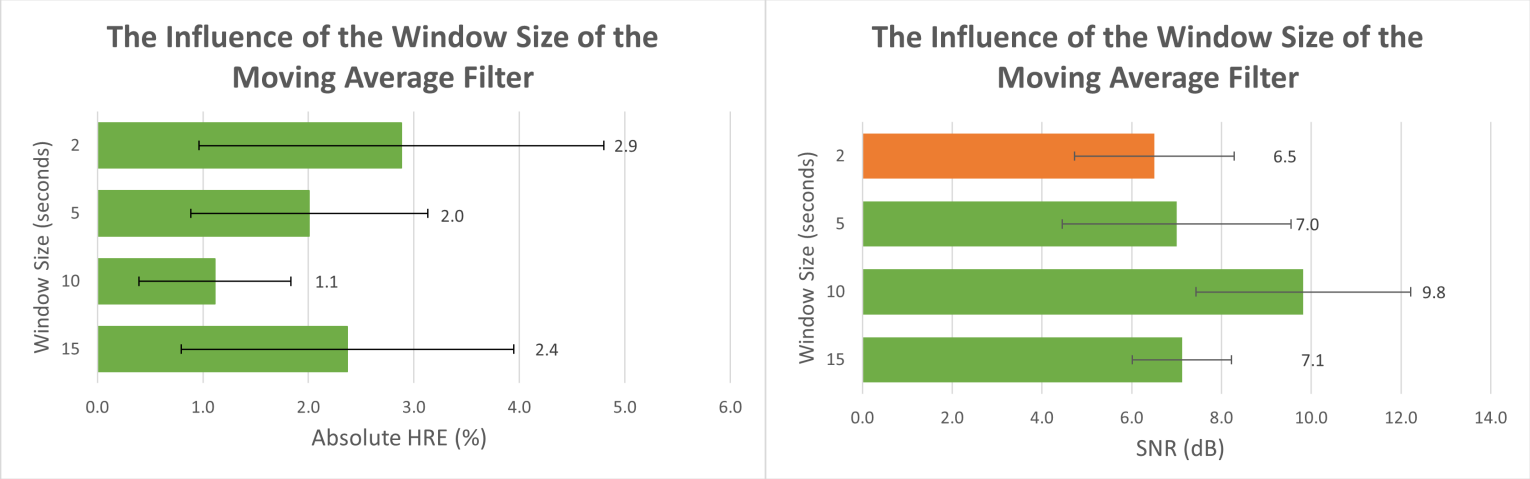

(a) The absolute HRE of the different window sizes

(b) The SNR of the different window sizes

Figure 44: The evaluation metrics of the window sizes of the moving average filter, where the x-axis and y-axis denote the evaluation metrics and the window size of the moving average filter respectively.

8.1.4 rPPG Algorithms

From the tested rPPG algorithms, the POS algorithm delivered both the lowest HRE and the highest SNR in both the ambient and the NIR conditions, see Figure 45 and 46. The p-value for the one-way ANOVA of the SNRa values between the POS method under ambient and under NIR conditions is P = .05.

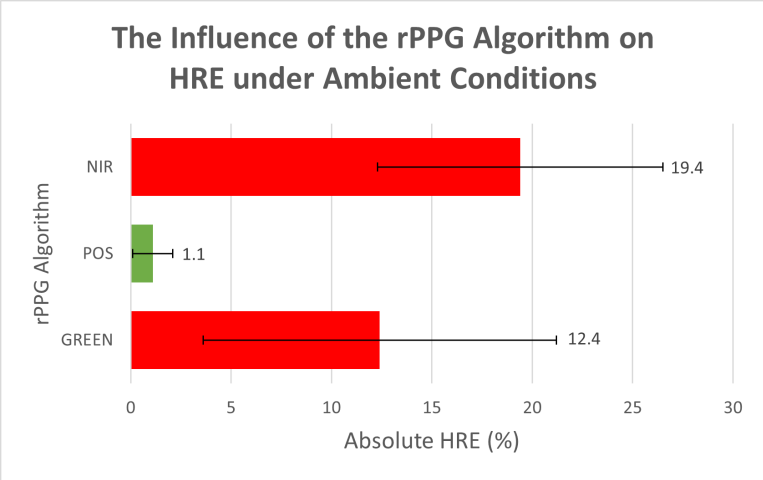

(a) The absolute HRE of rPPG algorithms under ambient conditions

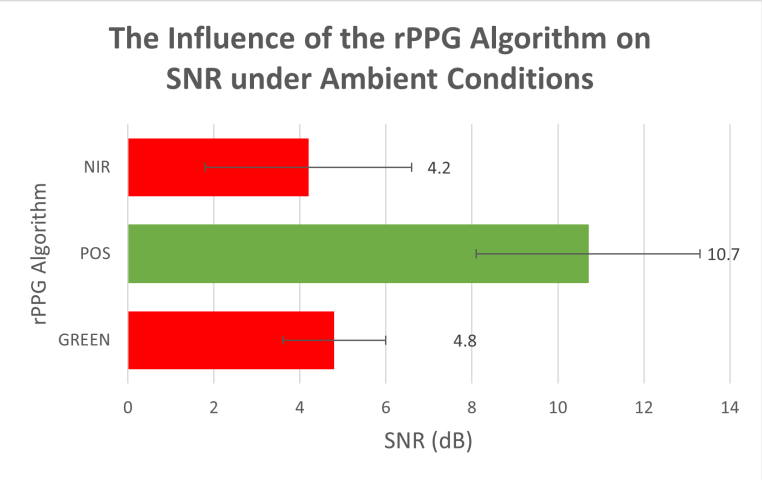

(b) The SNR of the rPPG algorithms under ambient conditions

Figure 45: The evaluation metrics of the rPPG algorithms under ambient conditions, where the x-axis and y-axis denote the evaluation metrics and rPPG algorithm, respectively.

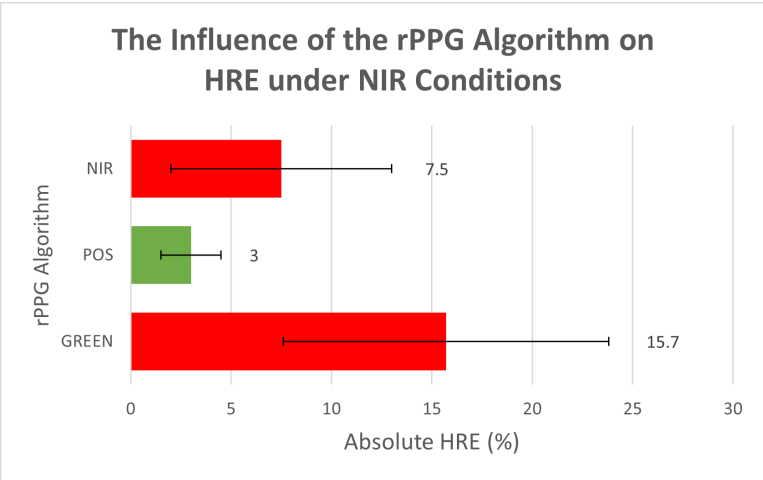

(a) The absolute HRE of the rPPG algorithms under NIR conditions

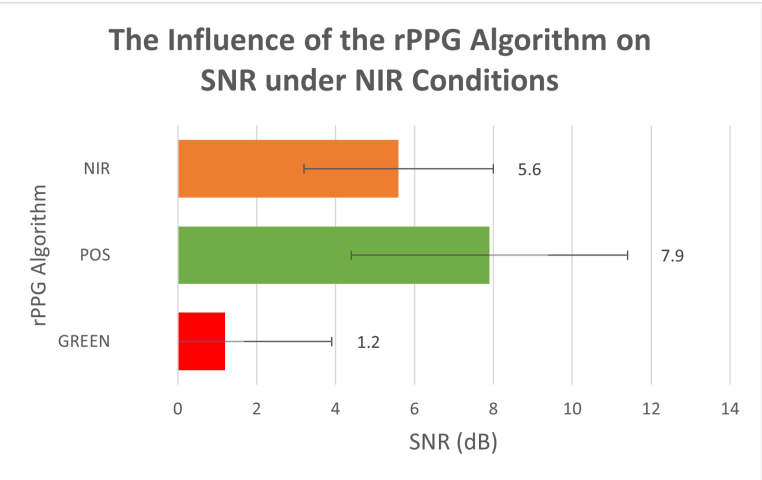

(b) The SNR of the rPPG algorithms under NIR conditions

Figure 46: The evaluation metrics of the rPPG algorithms under NIR conditions, where the x-axis and y-axis denote the evaluation metrics and the rPPG algorithm, respectively.

8.2 Bland Altman plots of the NIR measurements

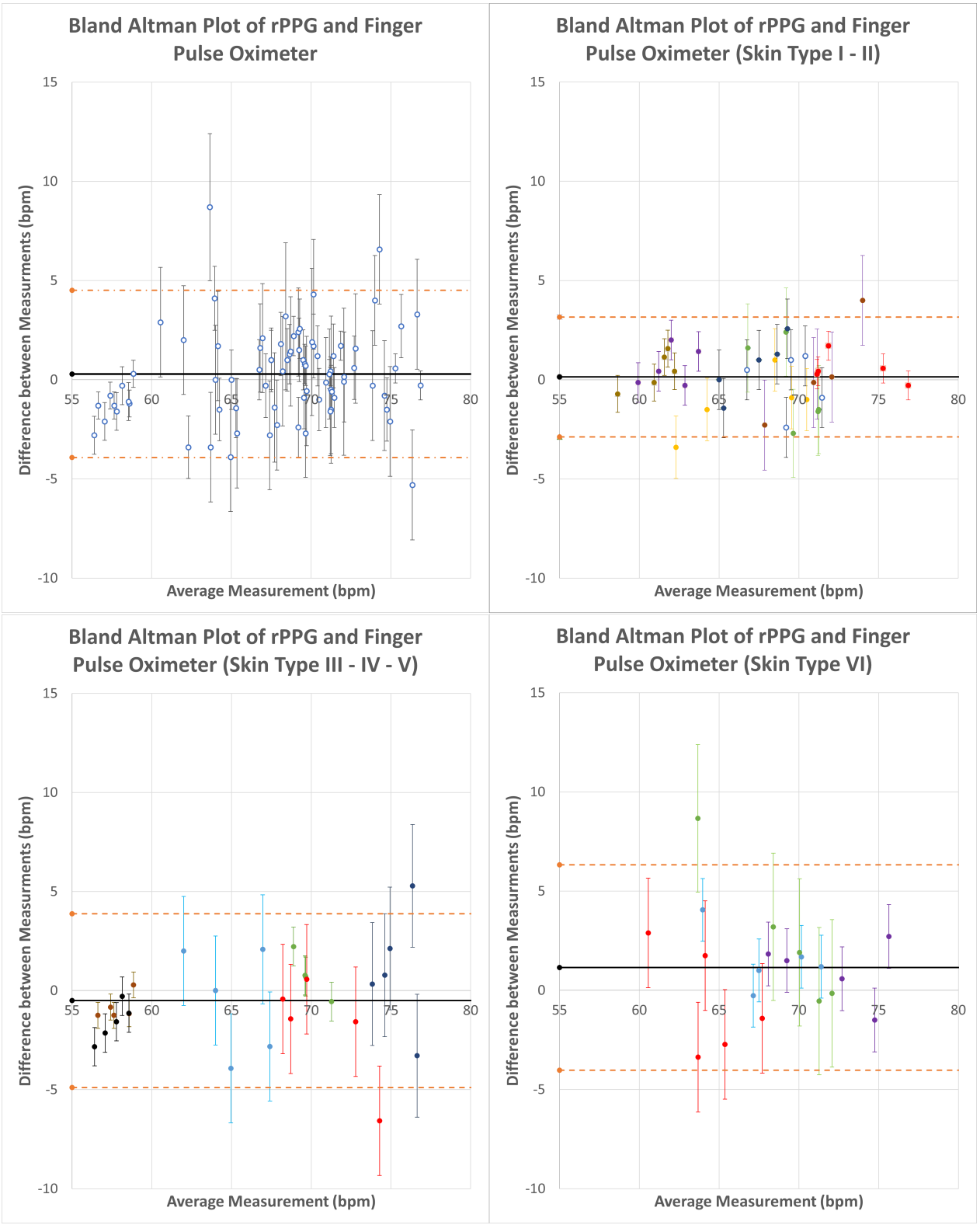

Figure 47: Bland Altman plots of the NIR-rPPG measurements.